Natural Resources
Canada

Ressources naturelles
Canada

GEOLOGICAL SURVEY OF CANADA
OPEN FILE 8553

Observation of bottom currents and sediment transport from the 2015–2016 year-long deployment of a seabed lander on the shelf edge of the Beaufort Sea, offshore Northwest Territories

M.Z. Li, E.L. King, D. Schillinger, A.G. Robertson, and Y. Wu

2019

Canada

GEOLOGICAL SURVEY OF CANADA
OPEN FILE 8553

Observation of bottom currents and sediment transport from the 2015–2016 year-long deployment of a seabed lander on the shelf edge of the Beaufort Sea, offshore Northwest Territories

M.Z. Li[1], E.L. King[1], D. Schillinger[2], A.G. Robertson[1], and Y. Wu[3]

[1] Geological Survey of Canada, 1 Challenger Drive, Dartmouth, Nova Scotia B2Y 4A2
[2] GaleForce Scientific Consulting Ltd., 2036 Bauer St., Halifax, Nova Scotia B3K 3W3
[3] Ocean Ecosystem Sciences Division, Department of Fisheries and Oceans, 1 Challenger Drive, Dartmouth, Nova Scotia B2Y 4A2

2019

Permanent link: https://doi.org/10.4095/314645

This publication is available for free download through GEOSCAN (http://geoscan.nrcan.gc.ca/).

Publications in this series have not been edited; they are released as submitted by the author

Table of Contents

Observation of bottom currents and sediment transport from the 2015-16 year-long deployment of a seabed lander on the shelf edge of the Beaufort Sea

Summary

Measurements of near-bed current and sediment transport on the Beaufort shelf break and upper slope are lacking. This limits our understanding of magnitude and frequency of bottom currents and seabed erosion and in particular whether these are responsible for the observed erosion and non-deposition of modern sediments on the Beaufort shelf edge and upper slope. Two instrumented tripods with limited sensor packages and process-dependent sampling methods were respectively deployed on the Beaufort shelf break and upper slope from August 2015 to August 2016. They were deployed for long term observation of bottom currents, and suspended sediment concentration as well as temperature and salinity. This experiment thus represents the first ever year-long under-ice deployments of seabed landers in the deep water depths of the Beaufort Sea. Both tripods were equipped with a Nobska Modular Acoustic Velocity Sensor (MAVS) current meter, a Nortek Aquadopp acoustic Doppler current profiler (ADCP), a Conductivity-Temperature-Depth (CTD) sensor, and two optical backscatter sensors (OBS) attached respectively to the MAVS and the ADCP instruments. The tripod on the shelf break was recovered on 31 August 2016. Efforts to retrieve the tripod on the upper slope, however, were not successful.

MAVS4D and attached OBS recorded data from 8/27/2015 to 7/20/2016. Aquadopp ADCP and attached OBS recorded data from 8/27/2015 to 8/31/2016. SeaBird CTD worked from 8/27/2015 to 9/11/2016. The OBS data obtained in this deployment were of poor quality. The OBS on ADCP likely failed after 10 November 2015. Data from the MAVS OBS looked suspicious after 3 May 2016 likely attributed to bio-fouling. Roll, pitch and compass data suggest that the tripod was stable through the deployment duration, although the frame settled ~10 cm into the soft muddy sediments on the shelf break. Temperature varied between 0.5 to -2 degrees from September 2015 to early May 2016, and after that time the temperature stayed constant at approximately -2 degrees.

The vertical profiles of velocity and backscatter intensity from the Aquadopp ADCP demonstrate short bursts of strong northeastward currents that extended through the entire bottom boundary layer of ~1 m and were typically associated with increased backscatter (sediment concentration). The ADCP measurements also show occurrences of bottom-confined (<0.3 m above bottom (mab)) current events which were not associated with any increase of backscatter intensity. The profiles of the velocity components averaged over the deployment duration give a northeastward residual current of ~6 cm/s. The mean vertical velocity was ~4 cm/s indicating that downwelling condition was dominant for the deployment period. The 1-min averaged current data recorded by the ADCP at 1 m above bottom (mab) indicate frequent occurrence of strong bottom currents

that reached a maximum of ~60 cm/s. The 2.5-min averaged bottom currents recorded by the MAVS were even stronger and gave a maximum of 1.1 m/s likely due to MAVS sampling a smaller volume at a higher frequency. The direction of the strong currents was dominantly to the northeast. The periodic occurrence of strong currents caused seabed erosion ~14% of the time over the year-long deployment on the Beaufort shelf break.

Qualitative correlation between the ADCP backscatter and the suspended sediment concentration (SSC) measured by the OBS sensors was observed lending some confidence of the usefulness of the OBS data. The backscatter data recorded by the ADCP were good through the entire deployment duration and showed qualitative correlation with the peaks of bottom currents. The ADCP backscatter and the OBS data both demonstrate periodic resuspension of bottom sediments. Maximum SSC of the OBS data were ~40 mg/l at 1 mab and reached ~150 mg/l at 0.5 mab. The backscatter intensity during strong current events reached up to ~60 arb. dB and were ~35 arb. dB higher than the background value. The increase of backscatter extended through the entire bottom layer, and was the strongest immediately above the seabed and decreased with the increase of height above bottom.

Spectral analysis of the hourly mean current speed and velocity component data suggest that the energy at the tidal frequencies (12 and 24 hours) was much lower than that at the lower frequencies at ~20 days and 1.5 months periods respectively. Energy also increased over the 2 - 5 day periods suggesting contribution from meteorological storms. The significant wave height and peak wave period data derived from the MAVS burst data look suspicious and likely indicate that the effect of waves was not significant in 168 m water depth along the shelf break. However, the spectra of the along and cross-shelf velocity components did show elevated energy at the swells (~15 s) and infra-gravity (>33 s) bands suggesting that these longer-period waves do have some impact on the seabed on the Beaufort shelf break.

Two distinctive types of current events were identified based on the velocity profile data recorded by the ADCP: Type ii depth-independent events in which increased currents extended through the entire bottom layer and Type iii bottom-intensified events in which the increase of current speeds was confined to the bottom ~0.3 mab. Depth-independent Type ii events are recognized in strong horizontal velocity throughout the bottom layer, current direction dominantly to the NE, increased backscatter and little change of vertical velocity. Bottom-intensified Type iii events, however, are mainly shown by strong horizontal shear between the horizontal currents of the upper and lower bins, variable or clock-wise rotating current direction, large near bottom vertical velocities and non-correlation with the increases of backscatter intensity. Bottom intensified Type iii events are also generally associated with large-amplitude temperature changes while temperature changes for Type ii current events were characterized by high frequency but low amplitude variability. The occurrences of Type ii and Type iii events were mutually exclusive. Type iii events mostly occurred over the ice-covered winter months

while Type ii events seem to occur throughout the year, but events with the strongest currents mainly occurred in the late spring and summer of 2016. The bottom-intensified Type iii current events represent an unusual phenomena as they were confined close to the seabed, energetic and yet causing little increase of backscatter intensity. The cause of these unusual bottom-confined strong current events should be further explored in future research.

1. Introduction

Limited wind-driven current modelling (Williams and Carmack, 2010) and current mooring measurements (Forest et al., 2007, 2008; Li et al., in review) suggest that much strong currents occur on the Beaufort shelf edge and upper slope. Oil and gas industry expressed concerns on how current strength and seabed instability may constrain their exploration and production operations. On-going research at the Geological Survey of Canada-Atlantic (GSCA) shows that some of the massive failures on Beaufort slope display little or no post-slide sediment record, and that an erosional and non-deposition zone exist on the Beaufort shelf edge and upper slope (King et al., 2017). It is speculated that the strong bottom currents may be responsible for the erosion and non-deposition of modern sediments on the Beaufort shelf edge and upper slope (Li et al., in review). Most mooring studies, however, typically targeted current measurements in the water column 10s to 100s m above seabed. Knowledge of near-bed current intensity and occurrence of sediment erosion and transport on the Beaufort shelf break and upper slope is lacking. A sediment transport component was developed in the Beaufort Sea Geohazards Assessment (BSGA) Activity within the GSC Public Safety Geoscience Program to address these issues. One of the principle goals of the sediment transport sub-activity in BSGA is to determine the magnitude, frequency and driving mechanisms of bottom currents and sediment transport on the Beaufort shelf edge and upper slope through deployments of instrumented seabed landers. The knowledge of bottom currents and sediment erosion would contribute to the overall goal of improved understanding of deep-water geohazards on the Beaufort Slope through (1) determination of the shelf to upper slope sediment fate and (2) the contribution to the assessment if shelf edge and deep-water landslides, mud volcanoes and shelf-edge deformation features are active or relic.

As part of the sediment transport sub-activity of BSGA, two instrumented seabed landers were deployed on the shelf break and upper slope of the Canadian Beaufort Sea during the Amundsen 2015804 Expedition (Figure 1). Several factors contributed to the selection of the deployment locations, suite of sensors mounted on each lander, and the deployment and sampling strategies for the 2015-16 seabed lander deployment in the Beaufort Sea. Limited current mooring data have been compiled and compared with the grain size data to derive preliminary understanding of the intensity, frequency and spatial patterns of near-bed currents and sediment mobility on the Beaufort Shelf break and upper slope (Li et al., in review). Analysis of acoustic survey data has recently confirmed the presence and mapped the spatial patterns of an erosional and non-

deposition zone on the Beaufort outer shelf and upper slope (King et al., 2017). Findings from these studies provided guidance for the location of the co-located deployments of seabed landers so that bottom currents and sediment transport processes would be simultaneously observed along a cross-slope transect from the shelf break to the upper slope. The selection of the deployment locations also considered the closeness to the 2015 ArcticNet/Golder mooring site on the central Beaufort Slope (Fig. 1) so that oceanographic processes can be concurrently measured through the entire water column and that the bottom boundary layer measurements by our landers can be placed in a broader context to strengthen the process interpretation from the lander data. Previous oceanographic studies (e.g. Forest et al., 2015) and recent regional synthesis of existing mooring data (Li et al., in review) have demonstrated strong seasonality of near-bed current intensity and driving oceanographic processes which would require long-term deployments of seabed landers. These aforementioned factors necessitated a year-long study using concurrent observations from two simplified seabed landers. Two instrumented tripods with limited sensor packages and intelligent sampling methods were respectively deployed on the shelf break (lander shallow; Figures 1 and 2) and the upper slope (lander deep) from 27 August 2015 to 11 September 2016 for long term observation of bottom currents, suspended sediment concentration as well as temperature and salinity for the deep-water setting in the Beaufort Sea. This experiment represents the first ever year-long under ice deployments of GSCA seabed landers in relatively deep water depths. The objectives of this report are to describe the instrumentation and field activity of the seabed landers deployed, provide assessment of sensor performance and the data quality, and present preliminary finding on the intensity and frequency of bottom currents and sediment erosion on the Beaufort shelf break and upper slope.

2. Instrumentation and Deployment Location

2.1 Deployment location

Two instrumented seabed landers (tripods) were deployed on 29th August 2015 during CCGS Amundsen 2015804 expedition. The first seabed lander (lander-shallow) was deployed at 01:08 29th August on the central Beaufort Shelf break in 168 m water depth at 70.8361° N 135.1294° W (Figure 1 and Figure 2a). The site was over local smooth mud deposition in "freestream" between the pingo-like features (PLFs). The deeper seabed lander was deployed at 02:51 in 185 m of water over much smoother topography on the uppermost slope at 70.8689° N and 135.0191° W (Figure 1 and Figure 2b). The deep lander was located just ~500 m down-stream to the northeast of the ArcticNet mooring BR-K site. The selection of the deployment locations of the two seabed landers, in association with the mooring at BR-K, aimed to obtain simultaneous observation of bottom currents and sediment transport processes along a cross-slope transect from the shelf break to the upper slope.

A conductivity, temperature and depth (CTD) cast with Rosette water sampler and an lowered acoustic Doppler current profiler (LADCP) was also performed near the shallow lander site (70.8358° N, 135.1300° W) at 23:30 on 28th August that provided temperature, salinity and velocity data in the water column at the time of deployment. Following the CTD-Rosette cast, a box core was taken at 23:58 near the shallow lander site (70.8357°N, 135.1305°W; Figure 2a). A box core was also taken for the deep lander site at 01:17 on 29th August (70.8703°N, 135.0275°W; Figure 2b). Push cores, surface samples (0 – 3 cm) and bulk mixed samples of approximately 5 kg (Figure 3) were taken from both box cores respectively for geotechnical property analysis, grain size analysis and sensor calibration purposes. The photos of the box core surfaces in Figure 3 suggest fine-grained sediments at both sites. Laboratory analysis showed that surficial sediment (0 – 3 cm) at the shallow lander site has a mean grain size of 0.014 mm (fine silt) with 30.6% sand, 36.4% silt and 33.0% clay. The surficial sediments at the deep lander site shows a mean grain size of 0.0059 mm (very fine silt) with 10.6% sand, 46.5% silt and 42.8% clay.

2.2 Instrumentation

The sensors and sampling strategies differed on the two seabed landers due to the difference in water depths and possible prevailing oceanographic processes. The sensors on the shallow lander (Figure 4; Table 1) on the shelf break included a Nobska MAVS4D (Modular Acoustic Velocity Sensor; S/N: 10292) travel time current meter that was centrally located on the frame in a downward orientation with a probe height of 100 cm above bottom (cmab). A Seapoint optical backscatter sensor (OBS; S/N: 12774) was attached to the MAVS and secured to the inside of a leg at 100 cm height. A Nortek Aquadopp 2 MHz ADCP with right angle head and 200 m pressure transducer (S/N: AQD6706/ASP4061) was positioned horizontally in a downward orientation at a height of 155 cmab. A D&A OBS sensor (S/N: 8524) was attached to the Aquadopp and secured to the inside of a leg at 50 cmab. A SeaBird SBE-37 MicroCat Conductivity/Temperature/Depth (CTD) sensor (S/N: 375M40415-5341) was mounted at a height of 160 cmab. Given the 165 m water depth at the shallow lander site and possible impact on the seabed by long-period waves, the MAVS4D and associated OBS were programmed to burst sample for 2.5 min every 2.0 hrs at 2 Hz storing 300 samples. The burst sampling duration, frequency and intervals would allow the observation of long-period waves and infra-gravity waves. With a double lithium battery pack installed, the MAVS4D power consumption predictions estimated a deployment duration of over a year while memory constraints would limit the recording duration to approximately 11 months. To ensure year-round recording of data, the AquaDopp and associated OBS were programmed to run for 1.0 min every hour internally averaging to record 1 profile every hour using 10 cm cells and a 20 cm blanking zone (the immediate range from the transducer for which measurements could not be made). The AquaDopp would have no memory issues running for up to 1 year and with a double lithium battery pack the estimated battery usage for this period would be approximately 21% not

including the OBS drain. The SeaBird CTD was programmed to sample every 10 min and record the average of four samples.

The deep lander deployed on the upper slope consisted of a Nobska MAVS3D (S/N: 10209) travel time current meter that was centrally located on the tripod frame in a downward orientation with a probe height of 100 cmab (Figure 4; Table 2). A Seapoint OBS (S/N: 11067) was attached to the MAVS and secured to the inside of a leg at 100 cmab. A Nortek AquaDopp 2 MHz ADCP with right angle head and 500 m pressure transducer (S/N: AQD2666ASP2349) was positioned horizontally in a downward orientation at a height of 155 cmab. A D&A OBS (S/N: 8148) was attached to the AquaDopp and secured to the inside of a leg at 50 cmab. A RBR Conductivity-Temperature (CT) sensor model XR-420 (S/N: 15222) was mounted at a height of 160 cmab. The MAVS3D and associated OBS were programmed to run for 2.5 mins every 2 hours at 1 Hz storing 150 samples. With a double lithium pack installed the power constraints would allow the MAVS3D to run for well over a year while memory constraints limited the deployment duration to approximately 11 months. The AquaDopp and associated OBS were programmed to run for 1.0 min every hour internally averaging to log 1 profile every hour using 10 cm cells and a 20 cm blanking zone. The AquaDopp would have no memory issues running for up to 1 year and with a single lithium pack the estimated battery usage for this period would be approximately 43 % not including the OBS drain. The RBR CT was programmed to run in burst mode and record one sample every 30 min.

The seabed lander deployed on the shelf break was successfully recovered on 31 August 2016 during the CCGS Amundsen 2016805 expedition. The recovery of the upper slope seabed lander during that expedition failed. Another effort to recover the deep lander through collaboration with IOS during a 2017 expedition on CCGS Sir Wilfrid Laurier was also unsuccessful due to non-respondance of the acoustic release. Thus, the deep lander deployed in 2015 remains un-recovered on the Beaufort upper slope.

3. Ancillary Data, Initial Assessment and Quality Control

3.1 Post processing steps

Initial quality assessments determined that the pressure signal from the MAVS was 10 decibars less than the pressure signal from the Aquadopp ADCP and Seabird CTD for the period of time when all three sensors were on bottom. Examination of the pressure data recorded before the lander entered water showed that the pressure sensors of the ADCP and CTD read values of 0, while the MAVS pressure sensor did not. This confirmed that the pressure data from the ADCP and CTD were zeroed with respect to atmospheric pressure prior to deployment. The pressure data recorded by the MAVS were adjusted to match the readings from the SBE pressure sensor by adding 10 decibars to the original MAVS pressure data.

As shown in Figure 4, The MAVS was installed in a down-ward facing direction. The data quality assessments indicated that the MAVS current meter needed to have the direction of the east/west, and north/south velocity components reversed, and the sign of pitch and roll needed to be changed to match the coordinate system of the Aquadopp ADCP.

Both the D&A OBS connected to the Aquadopp ADCP and Seapoint OBS attached to the MAVS4D recorded the output in counts as read from the on-board analog to digital (A2D) converters. The bulk sediments collected from the box core at the deployed site on the Beaufort shelf break had not yet been used to calibrate the OBS's to convert the OBS data in counts to concentration in g/L. Calibration coefficients for fine sand from a 2003 deployment of a seabed lander on southeastern Sable Island Bank, Scotian Shelf (Li et al., 2017) were used to convert OBS counts to concentration in this report. OBS calibration is sensitive to the sediment size distribution so the OBS concentration values reported here are meant to show trends and approximate concentrations only.

3.2 Ancillary data and initial assessment

The profiles of temperature, salinity, and velocity measured from the CTD-Rosette cast near the shallow lander site are shown in Figure 5. The temperature and salinity data demonstrate the water mass structure at the time of lander deployment at the end of August 2015. A well-mixed surface layer exists from 0 – 10 m depths and is characterized by 2.2°C in temperature and ~27 PSU in salinity (Figure 5b). A stratification layer lies beneath the mixed layer from 10 – 20 m depths in which the temperature decreased sharply to ~0°C and the salinity increased rapidly to ~30 PSU. From 20 – 140 m lies the so-called Pacific Halocline layer that demonstrated gradual temperature change from 0 to -1.5°C and salinity change from 30 to 34 PSU. Another sharp change in temperature and salinity was observed from 110 – 120 m to the ~160 m, about 3 m above the bottom. In this near-bed layer, temperature became warmer steadily (from -1.5° to -0.7°C) while salinity first increased sharply from 120 to 130 m depths then more gradually towards the seabed. The velocity profile data from LADCP (Figure 5a) show vertical patterns that roughly correlate with changes demonstrated by the temperature and salinity data. The surface layer from 0 – 20 m depths was characterized by the dominance of the v (northing) component of ~ -12 cm/s (southward) and weak u (easting) component of ~ -1 cm/s (westward). The currents in the surface layer thus were ~12 cm/s to the south. In the intermediate layer from 25 – 110 m, roughly corresponding to the Pacific Halocline layer, the speed of the v component decreased to ±1 cm/s and the u component became positive (eastward) and its speed increased to ~5 cm/s. Currents in the intermediate layer thus were to the east at ~5 cm/s. In the bottom layer from 110 – 150 m depths, the u and v components were both positive and the magnitude increased to ~13 cm/s and ~21 cm/s respectively. This results in a maximum current speed of ~23 cm/s to the northeast. The velocity profile data thus seem to suggest a bottom-intensified

layer that approximately correlates with the increase of temperature and more saline water of the near-bed layer demonstrated by the temperature and salinity data.

Time series of pressure, heading, pitch, roll, and temperature for all three instruments are shown in Figure 6. Data from the Aquadopp ADCP is shown in blue, the SBE-37 CTD in red, and the MAVS4D in green. Immediately apparent in this figure is the early end date of the MAVS with respect to the other two sensors. Also, the pressure data from the MAVS has some temporal variations when compared to the pressure data from the other two loggers. In comparison to the temperature time signal, the pressure signal from the MAVS tracks temperature indicating that the temporal variations of the MAVS pressure signal is likely attributed to the MAVS pressure sensor not being temperature compensated. The pressure signal from the Aquadopp ADCP shows a range in depth from 167.7 to 168.8 m over the course of the deployment. This is likely a drift in the pressure sensor that could be as large as 0.5% of the full scale. Pressure from the SBE-37 should be used when analyzing the slowly time-varying processes given that the pressure signal on the SBE-37 was most stable over the deployment duration.

There was a large and rapid magnitude change in heading around 10 November 2015 where the heading first gradually increased from 4 to 8 degrees before an abrupt drop to 3 degrees (Figure 6b). Pitch and roll showed little changes and were constant throughout the course of the deployment suggesting that the lander frame was stable over the deployment duration and thus the rapid change in heading was not caused by the movement of the seabed lander. Examination of the OBS data indicates that this abrupt change in heading was likely caused by the electronic spike due to a step change in the OBS reading connected to the Aquadopp ADCP (*see* Figure 17). The temperature data from all three sensors track well, and show similar magnitudes. Temperature varied between -2 and 0.5 degrees from September 2015 to early May 2016, and after that time the bottom temperature stayed constant at approximately -2 degrees.

Pressure, temperature and conductivity recorded by the CTD are shown in Figure 7. Salinity and density were calculated from the CTD data using the seawater package for Matlab and are shown in the bottom two panels. As stated earlier, the temperature from the CTD varied between -2 and 0.5 degrees on monthly or higher frequencies throughout the course of the deployment. The salinity and density were well correlated with the changes of temperature. Increases of salinity and density are largely associated with increases of temperature and vice versa. The large-amplitude changes in temperature, salinity and density did not occur after early May 2016 likely, suggesting changes of water mass after that date.

Acoustic interference likely caused bias in the current data recorded by the lowest bins of the ADCP instrument. This will be discussed in section 4.1 when ADCP data are presented.

4. Near-bed Currents and Suspended Sediment Concentration Data

4.1 ADCP measurements

Figure 8 shows temporal variation of the vertical profiles of the three components of velocity, U component (east/west, top panel), V component (north/south, mid panel) and vertical component W (up/down, bottom panel). Positive is east, north and downward respectively for the three components. Range from the Aquadopp is indicated on the y-axis, while time is on the x-axis. The magnitude and direction of the velocity is indicated by the color bar, red indicating positive and blue indicating negative. The solid black line on each panel shows the depth of the furthest "good bin," or the bin below which the acoustic signal interfered with the sea floor. U and V show short duration bursts of large positive velocities which existed throughout the water column ~1 m above seabed (e.g. in mid May and mid July 2016). The frequency with which these bursts occur increased after 20 April 2016. These depth-independent bursts did not appear in the W component at the color scale indicated in this figure. There were bottom-confined (at ~1 m range from the transducer or 0 – 0.3 mab) bursts of positive (red) and negative (blue) velocities in all three components which occurred throughout the data set (e.g. on December 15 and in mid February 2016).

Plots of the acoustic backscatter intensity as a function of time (x-axis) and range (y-axis) are shown in Figures 9 and 10. Backscatter intensity is shown by the color scale and is used as a measure of quality control, particularly in assessing the affects of side-lobe interference from the ocean-sediment interface. Backscatter intensity is also a proxy of the abundance of suspended particles in the water column. Figure 9 presents the raw backscatter intensities from each of the three acoustic beams (1-3 from top to bottom respectively) measured in counts. Figure 10 shows the backscatter intensity in arbitrary decibels (arb. dB) using a conversion factor of 0.4 dB/count and slant-range corrected to account for spherical spreading and attenuation losses along the path. Figures 9 and 10 both show intermittent periods of high levels of backscatter throughout the water that were qualitatively correlated with the depth-independent current events shown in Figure 8. Current events confined to the near-bottom layer of 0-0.3 mab, however, seemed to have insignificant effect on the backscatter intensity. Of note, the backscatter signal is slightly elevated in the bin above the seafloor, which is shown here by the high intensity backscatter at 1.4 m range.

Figure 11shows the backscatter intensity in arb. dB for beam 1 (upper plot), and the distance to the bottom for all three beams (lower plot). The distance to bottom was determined using a weighted peak detection algorithm applied to each time step of the acoustic data set. The algorithm is able to achieve a resolution of 10% of the cell size, or 1 cm in this case. The variations shown here are at the limit of that resolution but do indicate some deposition and erosion (up to ~2 cm) occurring beneath the frame. The three peaks displaying significant seabed changes of 12-14 cm in mid May, June and July 2016 were probably biased by the strong increase of backscatter intensity associated with energetic current events (Figures 8 and 10) and

should not be interpreted as real seabed elevation changes. The distance to bottom lines in the bottom panel of Figure 11 indicate that the ADCP height above bottom is 145 cm. As the Aquadopp was mounted at 155 cm above bottom, this difference thus suggests that the seabed lander frame settled ~10 cm into the muddy sediments.

The mean profiles of the backscatter and velocity components averaged for the deployment are plotted in Figure 12. The mean profile data show the effects of bottom interference more clearly when interpreting data quality. The height of the Aquadopp above bottom according to the log book is shown by the thick black line at a range of 155 cm. The mean backscatter at 1.4 m (bin 13 for 1.4 – 1.5 m range distance) showed an abrupt departure from the mean backscatter profile above suggesting that the cell of 1.4 – 1.5 m range was corrupted by the interference with the seabed and that the seabed should be between 1.4 to 1.5 m range distance. For the velocity components, the data at 1.3 m range (bin 12 for 1.3 – 1.4 m range distance) significantly deviated from the mean profiles above suggesting that the last good bin for the velocity data is bin 11 at 1.2 – 1.3 m range distance from the ADCP transducer. The profiles of mean backscatter indicate that the mean backscatter intensity was nearly constant (~33 arb. dB) in the water column except for a slight increase in the layer ~20 cm above the bottom. The mean U and V were also depth independent and both were ~4 cm/s giving a northeastward residual current of ~6 cm/s. The magnitude of mean U and V increased slightly in the bottom 30 cm. The mean of the vertical velocity was downward at ~4 cm/s and suggests that the bottom boundary layer was dominated by downwelling for the deployment period.

Time series of the 1-min averaged current speed in hourly intervals at 1 m above bottom, U100, and current direction recorded by the Aquadopp ADCP are presented in Figure 13. U100 frequently exceeded 30 cm/s and reached a maximum of ~60 cm/s. The direction of strong currents was dominantly to the northeast. Strongest currents (>40 cm/s) largely occurred in the summer of 2016 while magnitude and frequency of strong current events were approximately evenly distributed in other three seasons. Bottom currents (at 1 mab) were also recorded by the MAVS sensor. The comparison of the bottom currents from the ADCP and MAVS will be presented in the next section. According to Walker et al. (2008) and Li et al. (in review), the minimum threshold current speed (U100cr) for bedload transport for muddy sediments in the Beaufort Sea is ~19 cm/s (shown by the red lines in Figure 13). Comparison of the hourly 1-min averaged U100 measured by the Aquadopp ADCP with this threshold suggests that bottom currents caused bedload transport ~14% of the time for the year-long deployment in 2015-16 on the Beaufort shelf break. This is in agreement with the range of erosion frequency of 7 – 17% for the central Beaufort shelf break estimated from extrapolated legacy mooring current data (Li et al., in review). The estimated frequency of sediment erosion is corroborated by the qualitative correlation between backscatter intensity and bottom currents of the ADCP data presented in Figures 19 and 26 (*see* below).

4.2 MAVS measurements

Time series of the 2.5 min averaged current speed U100 and current direction recorded by the MAVS in 2-hour intervals are presented in Figure 14 (a, b). As demonstrated by the current data from the ADCP (Figure 13), the data from the MAVS also show frequent occurrence of strong bottom current events maximum velocity reaching up to 1.1 m/s. The direction of strong currents was predominantly to the northeast, although a secondary backflow to the SW was also detected. The occurrence of dominant and secondary current directions is better illustrated in Figure 14 (c, d) which presents U100 and direction for the period December 2015 to January 2016. The pairs of blue and red dashed lines respectively demarcate a current event with currents to the northeast and another event with currents to the south-southwest.

The bottom current U100 recorded by MAVS and the ADCP for the period 1 September 2015 to 20 July 2016 were compared in Figure 15a, b. The temporal variation patterns are well correlated. However, the current magnitudes recorded by MAVS were significantly higher than the data of ADCP. The differences between the bottom currents from MAVS and ADCP are further evaluated through the scatter plot of the U and V components (Figure 15c) recorded at 100 cmab by these two sensors. The U and V data for the MAVS were the averages of the first 120 points (for 1 min duration), while the ADCP data were resampled to the same time interval as the MAVS (1 per 2 hours). Again the magnitude and orientation (hence current direction) of the data point ellipses are in reasonable agreement with MAVS data showing higher values and bigger variations. This is likely attributed to the fact that the MAVS had a smaller sample volume and were sampled at a higher frequency (2 Hz), while the ADCP sampled at 1 Hz and averaged over a range bin of increasing volume with distance from the transducer.

The MAVS was programmed to burst sample at 2 Hz for 2.5 min every 2 hours (Table 1) in order to detect possible seabed impact of surface waves and infra-gravity waves. The burst data of pressure and velocity were used to estimate wave height, period and direction parameters. Significant wave height H_s and peak wave period T were calculated by computing the power spectrum for pressure and each velocity component for each burst recorded by the MAVS. Data were then multiplied by a frequency dependent correction factor to account for wavelength and depth-dependent attenuation. Summary wave statistics, together with current speed and the sediment concentration measured by the attached OBS, are shown in Figure 16. Significant wave height ranges from 0.3 – 0.7 m. Peak wave period ranges from 10 – 25 s but the data look suspicious. These likely suggest that effect of waves was not significant in 168 m water depth at the deployment site. Zoomed in check of the pressure data (Figure 6) does suggest that there were periods in which pressure oscillations increased moderately implying wave impact was detected near the seabed. This is supported by the minor energy peaks at the swell frequency (~15 s period) which will be discussed in Section 5.2. A casual correlation can be observed between current speed and sediment concentration recorded by the OBS which will be further

discussed in the next section. OBS data started drifting likely due to biofouling at approximately year-day 390 and became corrupted after year-day 460.

4.3 Suspended sediment concentration observation

The raw analog data (in counts) from the OBS sensors connected to the MAVS and Aquadopp ADCP instruments are presented in Figure 17. The OBS data collected in this deployment were of poor quality. Comparing data in Figure 17 b and c indicates that the OBS on ADCP likely failed after 10 November 2015. Data from the MAVS OBS looks suspicious after 3 May 2016, where the turbidity signal grows. The drift of the MAVS OBS was likely attributed to bio-fouling that occurred as the water mass changed after 3 May 2016.

The suspended sediment concentrations (SSC) converted from the analog data recorded by the MAVS and ADCP OBS sensors are shown in Figure 18 in comparison with the corrected acoustic backscatter from beam 1 of the ADCP instrument for the select time period 29 August to 21 January. The ADCP backscatter data demonstrated little differences between the heights of 0.5 and 1 mab. There is a qualitative correlation between the ADCP backscatter and the SSC measured by the OBS sensors. The peaks in SSC from the MAVS OBS at 1 mab in general correspond to the peaks of SSC measured by the ADCP OBS at 0.5 mab, although not all events at 0.5 mab were reflected in the concentrations at 1 mab. Events of increased SSC were periodically detected. Maximum SSC were ~40 mg/l at 1 mab and reached ~150 mg/l at 0.5 mab.

The backscatter intensity and the current speed U100 recorded by the ADCP for the entire deployment duration are compared in Figure 19a. The backscatter data were good for the entire deployment and show good correlation with the bottom current variations. The backscatter and U100 from the ADCP are compared with the SSC from the MAVS OBS at 1 mab for the select period of year-day 240 – 460 (September 2015 – March 2016) in Figures 19b, c to demonstrate the correlation between backscatter intensity and SSC from the OBS. The OBS data are generally correlated with the backscatter data. The correlated peak in mid- February and the low in late February in both the OBS and backscatter data (Fig. 19c) suggest that OBS data are useful up to February 2016. The drift and the spikiness of the OBS data after March make the data useless after that time.

5. Analysis of Current and Sediment Erosion Events

5.1 Identification, selection and description of Type ii and Type iii events

Temporal changes of temperature and salinity shown in Figure 7 and of bottom currents shown in Figures 13 and 14 are likely event driven. While the wave parameters derived from the analysis of the MAVS burst data (Figure 16) suggest that the impact on the seabed from surface

gravity waves was not significant, the time series of current speed data (Figures 13 and 14) and colour plots of velocity profiles (Figure 8) show that there were numerous current-driven events throughout the year.

Figure 20 shows a colour plot of speed (top panel) and direction (bottom panel) as recorded by the Aquadopp ADCP profiler. The ADCP was included on the lander to record velocity profiles in the bottom boundary layer with a sampling protocol designed to resolve low frequency events. Thus the data from the ADCP were principally used here to identify and describe these low frequency events. The time series of the color-coded vertical profiles of current speed in Figure 20 demonstrate the occurrence of dominantly two types of current events. One type was events in which increased currents extended through the entire bottom layer of ~1.2 m above seabed (depth independent; e.g. at mid-July 2016). These were designated as Type ii events (with background conditions without any increase of current speeds being defined as Type i events). The other type was events designated as Type iii events in which the increase of current speeds was confined to 0.2 – 0.3 mab (bottom intensified; e.g. at mid-December 2015). The time series of ADCP current speed at 1, 0.5 and 0.2 mab are shown in the six panels in Figure 21 to further demonstrate the vertical changes of current magnitude, different times of occurrence and seasonal distribution of the Types ii and iii events. Current speeds in Type ii events generally showed slight but steady increase as a function of height above seabed, particularly so for the three strongest events A-C in the summer 2016 (Figure 21b). In contrary, the increase of current speed only occurred in the lowest 0.3 m for the Type iii events with no perturbation found in the upper profiles (events 1-3 in Figure 21a). The occurrences of Type ii and Type iii events were mutually exclusive from each other. At the times when Type iii events occurred, currents in the upper part of the profiles (0.5 and 1 mab) were always quiescent. Figures 20 and 21 also suggest that Type iii events were concentrated over the ice-covered winter months. While Type ii events seem to occur throughout the course of the year, events with the strongest currents mainly occurred in the late spring and summer of 2016.

Based on the vertical profiles of current speed data, three Type iii events (events 1-3) occurring in the first half of the data set and three Type ii events (events A-C) occurring in the later half of the data set have been selected for detailed analysis (Figure 22). The detailed vertical profiles averaged over a 48 hour window (bottom panels in Figure 22) show that the increased currents for the Type ii events (A-C) extended over the entire measured bottom boundary layer and that the current speeds increased with increasing height above the seabed. The maximum velocity reached 50 – 60 cm/s. The velocity profiles of the three Type iii events (1-3 in the left 3 panels) demonstrate that the velocity in the upper column was much lower than Type ii events but rapidly increased from ~0.9 m range distance towards the seabed. The maximum velocity also reached 50 – 60 cm/s in these Type iii events. Hourly time series of current magnitude and vector over a 48 hour window for these selected events are presented in Figures 23 and 24 at 1 and 0.35 mab respectively. The hourly time series data corroborate the finding derived from the mean

vertical profile data that current speeds increased substantially at 0.35 mab in the Type iii events 1-3, while current speeds only changed slightly at these two heights in the Type ii events A-C. Currents were predominantly to the NE for Type ii events, while the direction of currents for Type iii events were quite variable and even rotated clockwise (event 2 in Figure 23).

Current speeds and backscatter responses for Type ii and Type iii events

Temporal variations of the corrected backscatter intensity (BS in arb. dB) at 0.2, 0.5 and 1.2 mab from the ADCP (Figure 25) demonstrate periodic occurrences of increased backscatter intensity that reached up to 60 arb. dB and were ~35 arb. dB higher than the background mean value. The increase of backscatter extended through the entire bottom layer and the events were well correlated at different heights above the seabed. For the events of increased backscatter, the backscatter intensity was the strongest immediately above the water-sediment interface and decreased with the distance away from the seabed.

Time series of backscatter intensity is compared with current speed at 0.2 and 1 mab in Figure 26. Events of increased backscatter intensity are shown to be mostly associated with strong currents of Type ii events, e.g. at year-days 300, 502, and 568. Strong currents of bottom-confined Type iii events, on the other hand, are not associated with increases of backscatter intensity, e.g. at year-days 353, 364, and 410. The differences in the correlation between currents and backscatter intensity for Type ii and Type iii events demonstrated here by individual events of the time series data are also found in the mean current and backscatter profiles which are presented in Figures 32 and 33 (*see* below) and discussed in the next section.

Based on the SW-NE orientation of the shelf edge bathymetry and the direction of upwelling-favorable and downwelling-favorable winds, several previous studies (Forest et al., 2015; Williams et al., 2008) have rotated the easting and northing velocity components 38° counter clockwise so that the down-shelf is toward the NE (52°T) and the down-slope is to the NW (322°T). The rotated coordinates will better define the along- and cross-shelf currents according to the orientation of the shelf edge bathymetry. Temporal variations of the vertical profiles of the rotated along-shelf and cross-shelf velocity components, as well as vertical velocity, temperature and backscatter intensity, are presented for the entire deployment duration in Figure 27 and for three months periods in Figures 28 – 31 respectively. Evaluation of Figures 27 – 31 demonstrates several non-periodic behaviours. Temperature oscillated from -2 to 0 degrees throughout the first 8 months and stayed relatively steady after that (Figure 27). Type ii depth-independent events are recognized in strong horizontal velocity throughout the bottom layer, increased backscatter and little change of vertical velocity. Bottom-intensified Type iii events, however, are mainly shown by strong horizontal shear between the horizontal speeds of the first bin (0.2 m from the transducer) and the 10th bin (1.1 m from the transducer), large near bottom vertical velocities, and non-correlation with the increases of backscatter intensity. Type iii events with strong down-

shelf velocity are associated with increased downward vertical velocity in downwelling conditions (mid-late December and on January 31 in Figure 29). Type iii events with strong up-shelf velocity seem to be associated with negative (upward) vertical velocity under upwelling conditions (on 15th and 30th of December in Figure 29). Large-amplitude temperature changes were generally associated with bottom-intensified Type iii events, while temperature changes were characterized by high frequency but low amplitude variability for the depth-independent Type ii current events.

Mean profiles of current and backscatter for Type ii, Type iii and other time periods

Mean profiles of current speed and direction, velocity components (rotated 38° counter clockwise), and backscatter intensity averaged for the time defined as Type ii events, the time as Type iii events, and all other time not defined as either Type ii or Type iii events are respectively presented in Figures 32 and 33 for further insights of the characteristics of these two types of events under time averaged conditions. It is noted that while backscatter data for the 1.3 m bin were good, velocity data for this bin were corrupted by interference of the seabed; the velocity data at this bin were included just to demonstrate where seabed interference started and should be ignored in interpreting the velocity patterns near the bottom. For time-averaged conditions, events of Type ii can be characterized by the strongest currents in the water column that show a trend of slight decrease toward the seabed (Figure 32). The mean current speed was ~18 cm/s in the upper profile and decreased to ~15 cm/s near the seabed. The direction of the mean currents was to the NNE. In contrast, the mean currents for Type iii events and background conditions were much smaller (~3-4 cm/s) and both showed a trend of increasing magnitude from the upper profile to the seabed. The increase, however, was small for the background conditions and much more substantial for Type iii events with maximum speed reaching ~25 cm/s at 1.1 m range distance. The mean currents for both Type iii and background conditions were to the ENE.

The averaged backscatter values serve as another feature distinguishing Type ii and Type iii events. Type ii events are characterized by high mean backscatter values (> 40, Fig. 33 left panel), while those of Type iii have the lowest values (<30). The mean backscatter for the background conditions is ~32 arb. dB, intermediate between Type ii and Type iii events. The profiles of the mean along- and cross-shelf velocity components (middle panels in Figure 33) show that Type ii events are characterized by moderate down-shelf and off-shore mean velocities throughout the near-bed layer, while Type iii events and background conditions show small mean down-shelf velocity and nearly 0 cross-shelf velocity. Additionally the down-shelf velocity increased to >20 cm/s and the cross-shelf velocity decreased to -10 cm/s (on shore) at 1.1 m range for Type iii events resulting in significantly increased near-bed current speed shown in the left panel of Figure 32. The profiles of the mean vertical velocity for all three conditions (right panel of Figure 33) show a similar pattern that the mean vertical velocity was ~5 cm/s (downward) at 0.2 m range and decreased to ~4 cm/s at 0.9 m range. Over the lowest bins,

vertical velocity continued to decrease to ~3 cm/s for Type ii and background conditions. The mean vertical velocity for Type iii events, however, increased to ~6 cm/s indicating stronger downward vertical velocity during Type iii current events.

The bottom-intensified Type iii current events represent an unusual phenomena as they were confined close to the seabed, energetic and yet causing little increase of backscatter intensity (Figure 26). It was suspected that the strong currents in these events could be generated by the turbulence and acoustic interference of the lander frames during currents from certain direction. The heading from the ADCP was 4 degrees magnetic north (Figure 6) and thus the ADCP head pointed to the north (Figure 4). Therefor currents from the SE, S and SW sectors would likely generate stronger turbulence from the frame-flow interaction. Detailed examination of the time series current data at different heights (as presented in Figures 21) shows that moderate to strong currents with variable directions in many events did not cause intensification of currents in the bottom 0.3 m. The current speed and direction at various heights for the Type iii events highlighted in Figure 21 are listed in Table 3. The currents at 1 mab for these events were weak to moderate and came from variable directions. The intensified currents at 0.2 mab were to the NE but also to the SW. All these evidences suggest that disturbance from frame-current interaction likely was not the cause of the occurrence of the strong currents in the Type iii events. Further more Type iii events were often associated with large amplitude changes of temperature (Figures 27 and 29) suggesting that these observed Type iii events are likely real physical process that is occurring on the Beaufort shelf break. The cause of these unusual bottom-confined strong current events with no associated increase in suspended sediment concentration should be further explored in future research.

5.2 Relative energy contribution based on spectral analysis

The hourly mean data of u and v velocity components at 100 and 20 cmab, have been used to compute the spectral energy as a function of frequency cycles per day (cpd) which are shown in Figure 34. Measurements at both heights show that although there are local energy peaks at the tidal frequencies (at 12.4 and 24 hours), the energy at the low frequencies (>10 days) is much higher. Intermediate to these frequencies, weak local peaks can also be recognized at 0.2 cpd (5 days) and 0.5 cpd (2 days) frequencies, indicating contribution from meteorological storms with 2 – 5 day periods. Currents at 20 cmab have higher energy than that at 100 cmab as the maximum power of the former reached 300 $cm^2 d^{-1}$ and the latter was ~ 200 $cm^2 d^{-1}$. At 100 cmab, the v component (cross-slope direction) was stronger than the u component (along-slope direction) while the u component was slightly stronger than the v component at 20 cmab.

The hourly mean current speed at 100 cmab, U100, was used to calculate the continuous wavelet spectral (CWT) power to assess the spectral power variation as a function of frequency and time. The wavelet spectral power is shown in Figure 35 in comparison with the time series of U100.

The time series of average variance for 8 – 32 hours (including tidal frequencies of 12 -24 hrs; Fig. 35d) and that for periods > 32 hrs (Fig. 35e) demonstrate that the energy for tidal frequencies (12-24 hrs) is lower than that for lower frequencies, corroborating the patterns shown by the normal spectral analysis results (Figure 34). The energy at the tidal frequencies was generally distributed evenly throughout the 1-year deployment duration while the energy peaks for the low frequencies occurred dominantly in May to July 2016. The spectral power from joint frequency and time analysis is plotted in Figure 35b and the total spectral energy against the frequency for the entire data is shown in Figure 35c. They once again show that energy is minimum at the tidal frequencies (12 and 24 hours) and that energy peaks occurred at ~20 days and 1.5 months periods respectively. The largest energy peak at 12 months is not valid as data for that peak were outside the 5% confidence level. Fig. 35b and c also demonstrate that energy also increased over the 2 - 5 day periods as it built toward the peak at the 20 day period. The occurrence of the energy patches in the 2 – 5 day periods is marked by the arrows in Fig. 35b.

The energy distribution for higher frequencies (>10^{-2} Hz) is examined by looking at the spectra calculated from the burst data from the MAVS. While the water depth of 168 m limits the effects of the short period waves on the pressure and velocity signals through attenuation, the longer period infra-gravity waves (periods > 33 s) can be characterized. The MAVS was set to sample at 2 Hz for 2.5 minutes (300 samples for 150 seconds). Using a 128 point fast Fourier transform with 50% overlap, spectra were calculated for the along- and cross-shelf components of velocity. Each burst was detrended before applying the spectral analysis to remove the mean and linear trend using Matlab's "detrend" function. Various mean spectra are shown in Figure 36.

The mean of the sum of the spectra of the along and cross-shelf velocity components in Figure 36a indicates that the mean energy is much stronger for the period after April 1, 2016 which could be expected from the more frequent occurrence of stronger current events in the latter part of the deployment shown in Figures 8 and 14. The sum of the spectra of the along and cross-shelf velocity components measured at 1 mab have been binned into percentiles. The spectra for times when the energy is below the 90th percentile and for those periods when the energy is in and above the 90th percentile presented in Figure 36b demonstrate that the energy was predominantly concentrated in the top 10% energetic periods as energy contained in these periods was approximately 2 orders of that in the bottom 90% energetic periods. The lower two plots of Figure 36 show respectively the mean spectra of along- (Fig. 36c) and cross-shelf (Fig. 36d) velocity components for periods defined as Type ii events, Type iii events and for time not defined as either Type ii or iii. Type ii events were defined as periods where the depth averaged backscatter intensity was above 40 arb. dB, while Type iii events defined as periods when the difference between the speed at 0.2 m range distance and 1.1 m range distance exceeded 20 cm/s. It should be noted that the strong currents of the Type iii events were confined in the near-bed layer 0.3 mab and the MAVS recorded current data at 1 mab. The potential contribution to the energy in the periods of 1 – 100 s from the bottom-confined Type iii events likely was not fully

captured. Figures 36c, d suggest that the energy of the along-shelf component was larger than the cross-shelf component at least for the period of Type ii events and the other time period. The spectra of the period after 1 April 2016 (Fig. 36a), the top 10% energetic period (Fig. 36b) and the cross-shelf component of the other time period (Fig. 36d) show elevated energy levels in the infra-gravity band (0.02 – 0.03 Hz). The spectra of the period after 1 April 2016 (Fig. 36a), the top 10% energetic period (Fig. 36b), and the along-shelf component of the other time period (Fig. 36c) also demonstrate elevated energy at the swells bands (0.07 Hz or ~15 s). Therefor waves in the swells and infra-gravity bands do have some impact on the seabed on the Beaufort shelf break.

Acknowledgements

References

Forest, A., M. Sampei, H. Hattori, R. Makabe, H. Sasaki, M. Fukuchi, P. Wassmann and L. Fortier, 2007. Particulate organic carbon fluxes on the slope of the Mackenzie Shelf (Beaufort Sea): Physical and biological forcing of shelf-basin exchanges, J. Mar. Syst., 68, 39-54, doi:10.1016/j.jmarsys.2006.10.008.

Forest, A., M. Sampei, M.-E. Rail, Y. Gratton and L. Fortier, 2008. Winter pulses of Pacific-origin water and resuspension events along the Canadian Beaufort slope revealed by a bottom-moored observatory, Proc. IEEE Oceans 2008, 10747934, 8 pp., doi:10.1109/OCEANS.2008.5152010.

Forest, A., Osborne, P.D., Fortier, L., Sampei, M. and Lowings, M.G., 2015. Physical forcings and intense shelf–slope fluxes of particulate matter in the halocline waters of the Canadian Beaufort Sea during winter, Continent. Shelf Res., 101, 1-21.

King, E.L., Li, M.Z., Wu, Y., Forest, A., Blasco, S., Harrison, P., Robertson, A., Melling, H., Dallimore, S.R., Paull, C.K., and Cameron, G.D.M., 2017. A belt of seabed erosion along the Beaufort Sea margin, offshore Northwest Territories, governed by Holocene evolution of the Beaufort Shelf-break Jet; geological evidence, current measurements, and initial oceanographic modelling; Geological Survey of Canada, Open File 8198, 1 poster. doi:10.4095/299691.

Li, M.Z., Prescott, R. and Robertson, A., 2017. Near-bed hydrodynamics and sediment transport processes at the head of Logan Canyon based on the 2005 lander deployment. Geological Survey of Canada, Open File 8174, 36 p. doi:10.4095/299794.

Li, M.Z., King, E.L., Forest, A., Melling, H., and Osborne, P.D., in review. Synthesis of near-bed currents and sediment mobility on the Beaufort Shelf edge and upper slope. GSC Open File xxxx.

Walker, T.R., J. Grant, P. Cranford, D.G. Lintern, P. Hill, P. Jarvis, J. Barrell and C. Nozais, 2008. Suspended sediment and erosion dynamics in Kugmallit Bay and Beaufort Sea during ice-free conditions. J. Mar. Syst., 74, 794–809, doi:10.1016/j.jmarsys.2008.01.006.

Williams, W.J. and Carmack, E.C., 2010. The effect of retreating summer ice on shelf-break exchange in the Arctic Ocean. Poster presentation in Ocean Sciences Meeting 2010, 22-26 February 2010, Portland, Oregon.

Williams, W.J., Melling, H., Carmack, E.C. and Ingram, R.G., 2008. Kugmallit Valley as a conduit for cross-shelf exchange on the Mackenzie Shelf in the Beaufort Sea. J. Geophys. Res., 113, p. C02007; doi:10.01029/02006JC003591.

Table 1 Types, heights, sampling strategies and duration of recorded data for sensors mounted on the shallow lander deployed in 2015-16 on the Beaufort Shelf break.

Instrument	Height (cmab)	Start Date & Time	End date & Time	Sampling Strategy	Notes
MAVS4D	100	8/27/2015 20:00	7/20/2016 20:00	2.5 min every 2 hrs at 2 Hz	Added 10 dbar to pressure sensor; Flip u, v; Flip pitch, roll.
Seapoint OBS	100	Same as above	Same as above	Same as above	
Aquadopp ADCP	155	8/27/2015 20:00:00	8/31/2016 21:00:00	Logged 1 min-averaged profile every hour	
D&A OBS	50	Same as above	Same as above	Same as above	
SeaBird SBE-37 CTD	160	8/27/2015 09:29:53	9/11/2016 01:09:52	recorded average of four samples every 10 min	

Table 2 Types, heights, and sampling strategies for sensors mounted on the deep lander deployed in 2015-16 on the Beaufort upper slope.

Instrument	Height (cmab)	Start Date & Time	End date & Time	Sampling Strategy	Notes
MAVS3D	100	N/A	N/A	2.5 min every 2 hrs at 1 Hz	The tripod has not been recovered yet.
Seapoint OBS	100	Same as above	Same as above	Same as above	
Aquadopp ADCP	155	N/A	N/A	Log 1 min-averaged profile every hour	
D&A OBS	50	Same as above	Same as above	Same as above	
RBR CT	160	N/A	N/A	record 1 sample every 30 min	

Table 3 Current speed and direction at 100, 50 and 20 cmab for selected bottom-intensified Type iii events observed with the shallow lander deployed in 2015-16 on the Beaufort shelf edge.

Year-day	U100 (cm/s)	Dir100 (degrees)	U50 (cm/s)	Dir50 (degrees)	U20 (cm/s)	Dir20 (degrees)
255.417	14.20	143	12.40	165	36.00	250
350.042	5.80	266	9.40	122	51.50	249
353.875	6.30	326	2.90	211	71.00	72
363.250	3.10	347	3.30	235	53.00	257
394.792	17.20	80	2.40	75	41.80	73
409.875	19.10	198	15.50	7	55.70	59
512.250	5.80	192	10.30	134	53.60	237
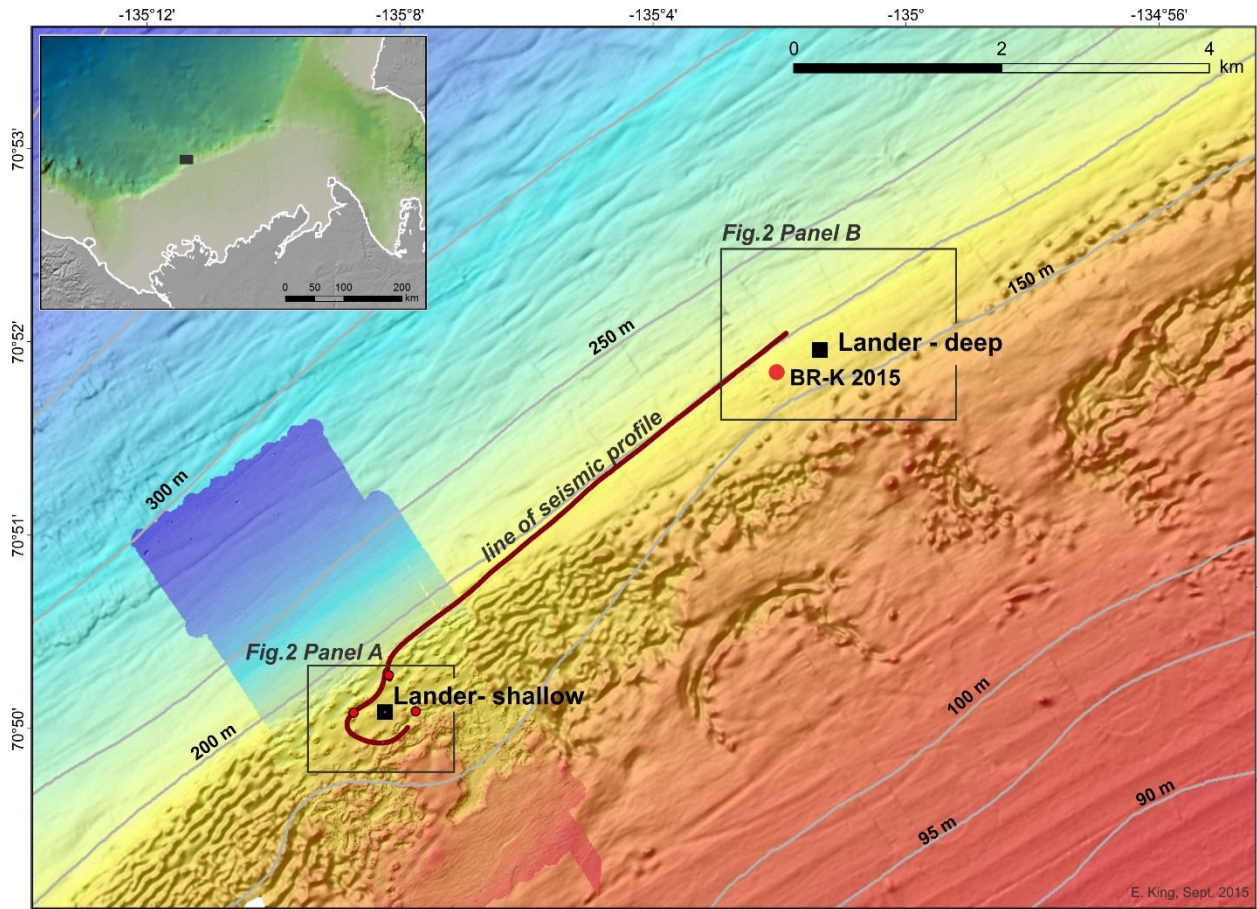
Figure 1 Map showing the locations of the seabed landers (squares) deployed in 2015-16 on central Beaufort Sea shelf break and upper slope in relation to the ArcticNet mooring site BR-K (red dot). Bathymetric contours (grey lines) are shown on the multibeam bathymetric image. The heavier brown line shows the line of seismic profile data that was used to help select the seabed lander deployment locations. Lander sites in Panels A and B are shown with greater detail in Figure 2.
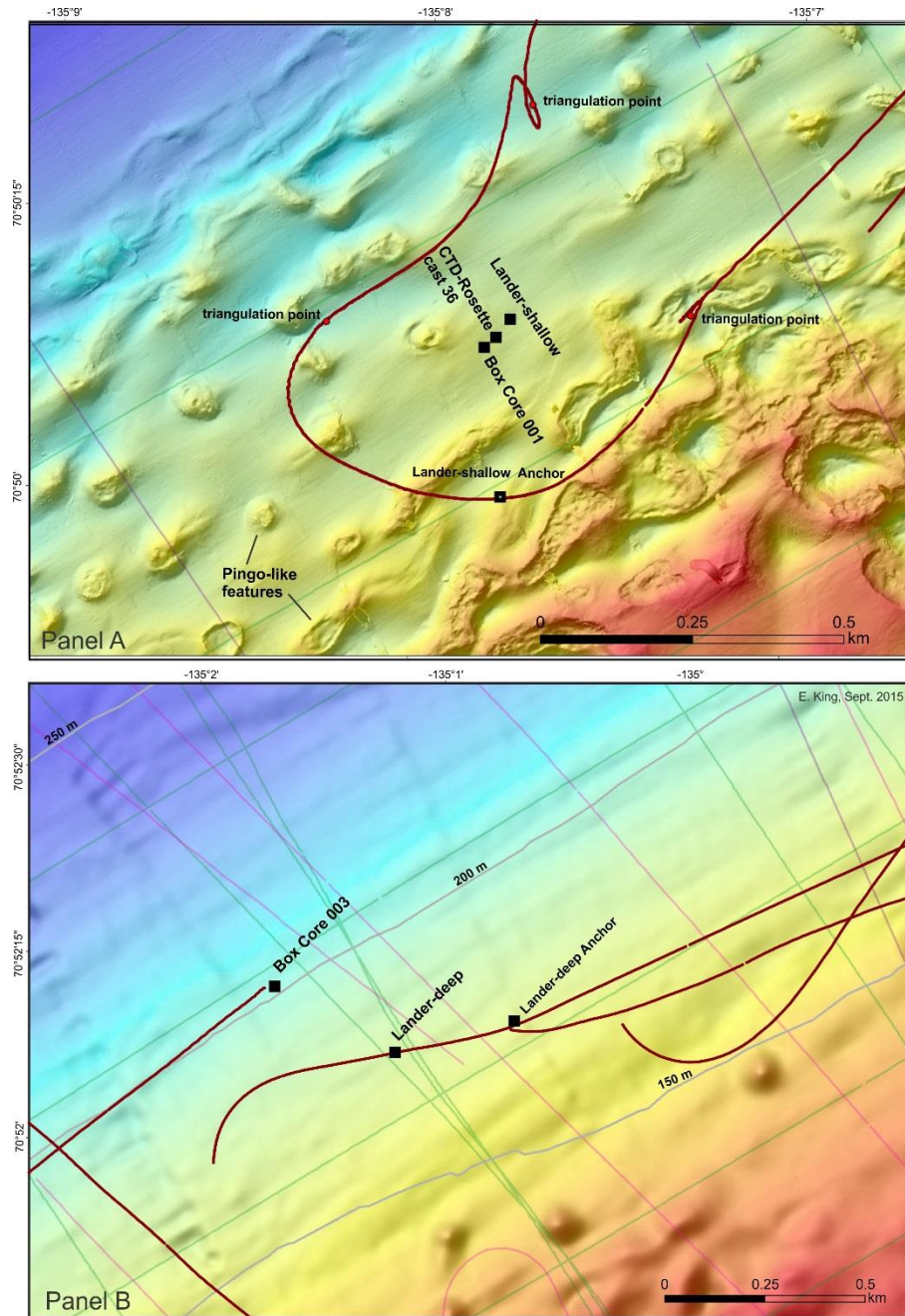
Figure 2 Close-up maps of (Panel A) the shallow lander location on the shelf break and (Panel B) the deep lander location on the upper slope. Subtle lines are existing 3.5 kHz sub-bottom profiler tracks and the heavier brown lines are the Amundsen 2015 tracks. The background image in Panel A is the high resolution Autonomous Underwater Vehicle (AUV) multibeam bathymetry rendering (courtesy C. Paull, Monterey Bay Aquarium Research Institute). This depicts local net mud deposition (smooth) surrounding and locally overlying pingo-like features (PLFs). The shallow tripod was placed in "freestream" between the PLFs. Panel B shows the much simpler topography of the uppermost slope near the deep lander. Weight anchor, CTD and box core sites are also shown.
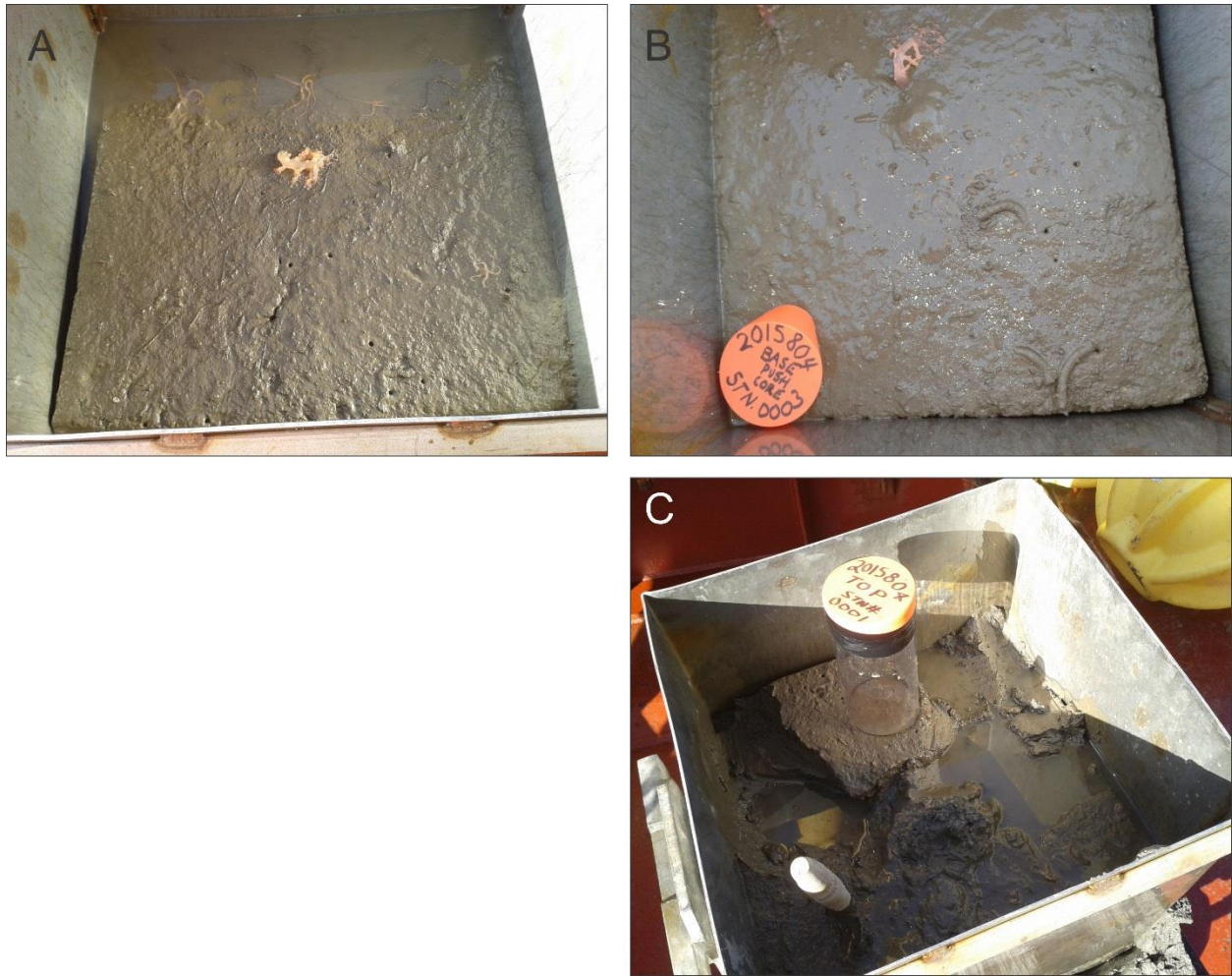
Figure 3 Seabed photographs from box cores recovered near the lander sites. Panel (A) shows the surface of the box core at the shallow lander site, panel (B) shows the box core at the deep lander site, and panel (C) depicts the push core extracted from the box core at the shallow site. Box is ca. 48 cm across.
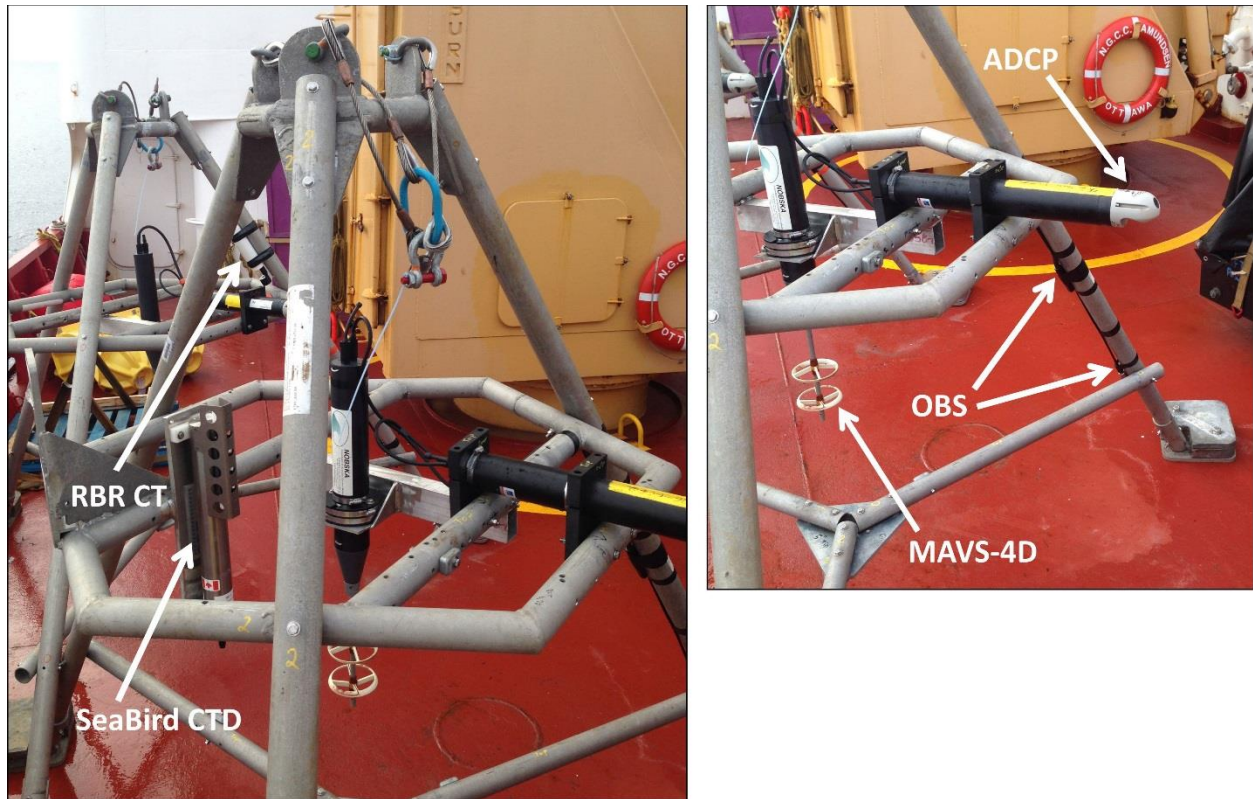
Figure 4 Photos of the instrumented tripods and various incorporated sensors for the Beaufort 2015-16 deployments aboard CCGS Amundsen. The shallow lander in the foreground (left photo) was equipped with a later generation of the MAVS-4D time-travel acoustic current meter and a Seabird Microcat CTD (conductivity, temperature and depth). The deep lander (in the background in left photo) was equipped with a MAVS-3D and a RBR CT (background). Both landers were mounted with the Nortek AquaDopp Acoustic Doppler Current Profilers (ADCP) and 2 Optical Backscatter Sensors (OBS).
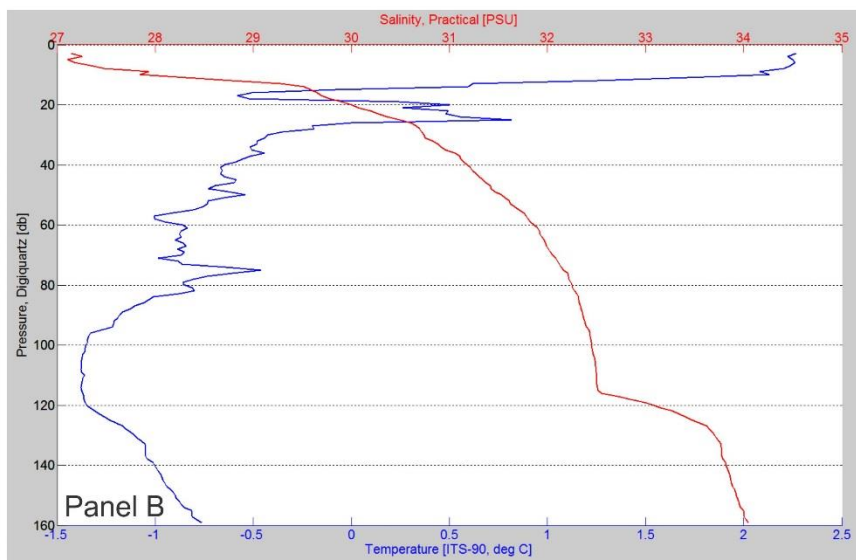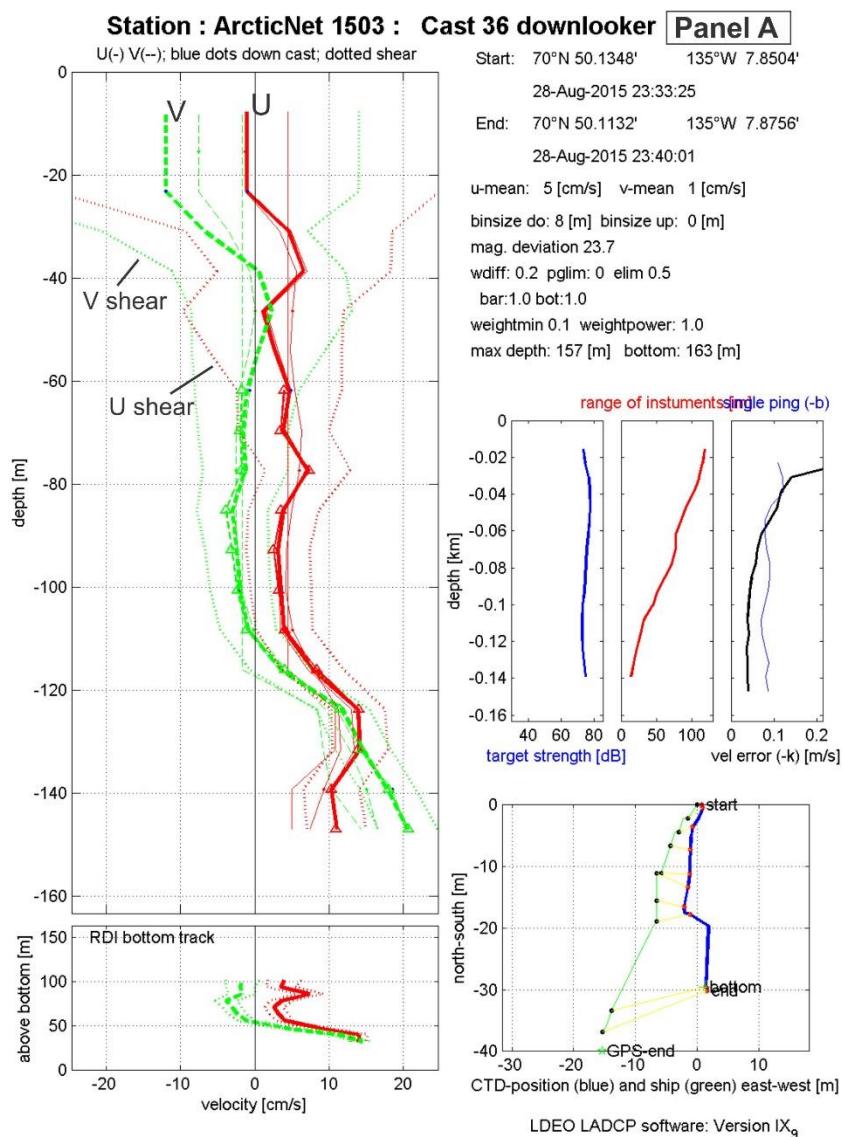
Figure 5 Plots of CTD-Rosette cast from nearby the shallow lander station (cast 36). (A) shows the profiles of the U and V velocity components and their shear recorded by the lowered Acoustic Doppler Current Profilers (LADCP). The thick solid red line and thick dashed green line are respectively the U and V velocity components. The dotted red and green lines represent respectively the range of the shear of the U and V components. (B) shows the vertical profiles of temperature (blue, °C) and salinity (red, ‰ or PSU).
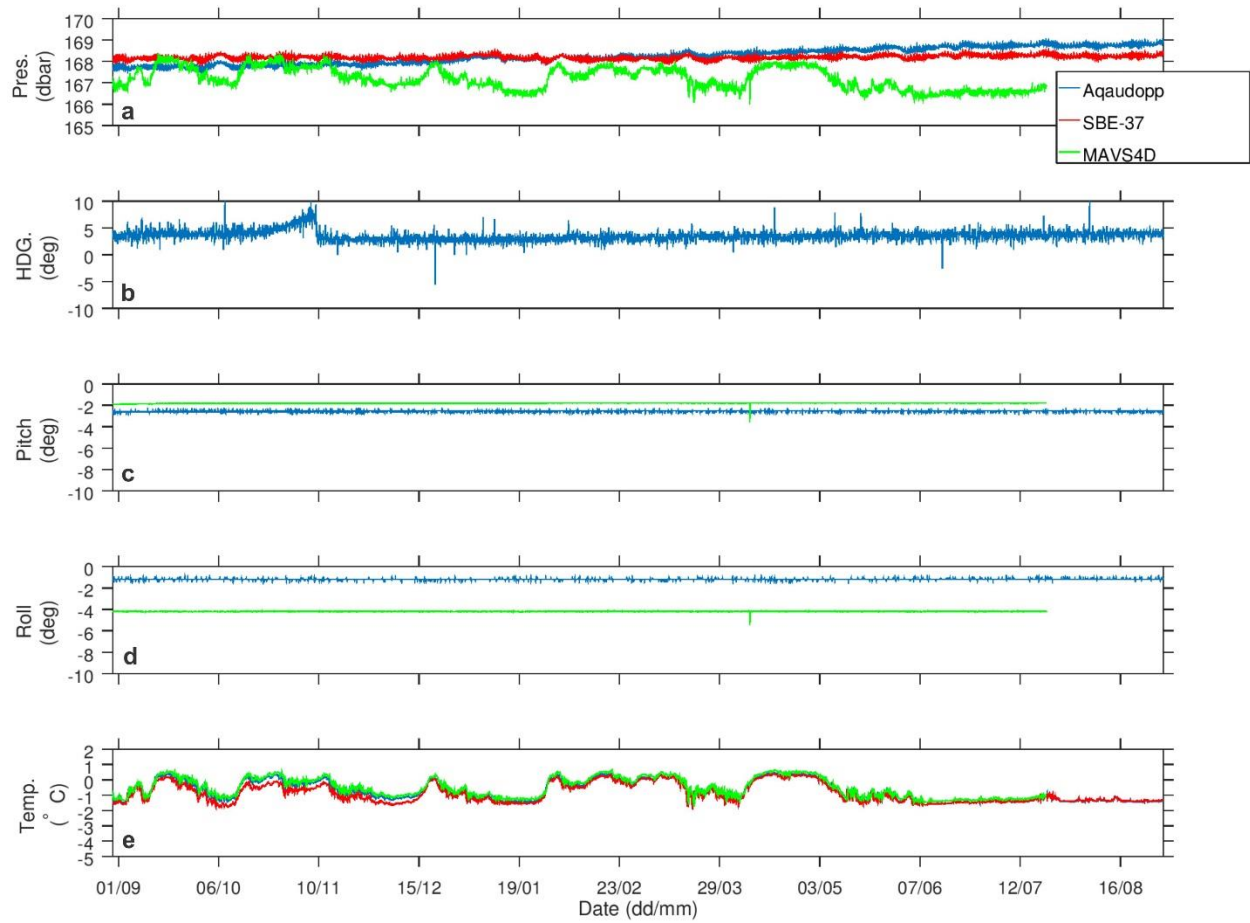
Figure 6 Time series of (a) pressure, (b) magnetic compass heading, (c) pitch, (d) roll and (e) temperature measured by the Aquadopp ADCP (blue), SBE-37 CTD (red) and MAVS4D (green) on the shallow seabed lander.
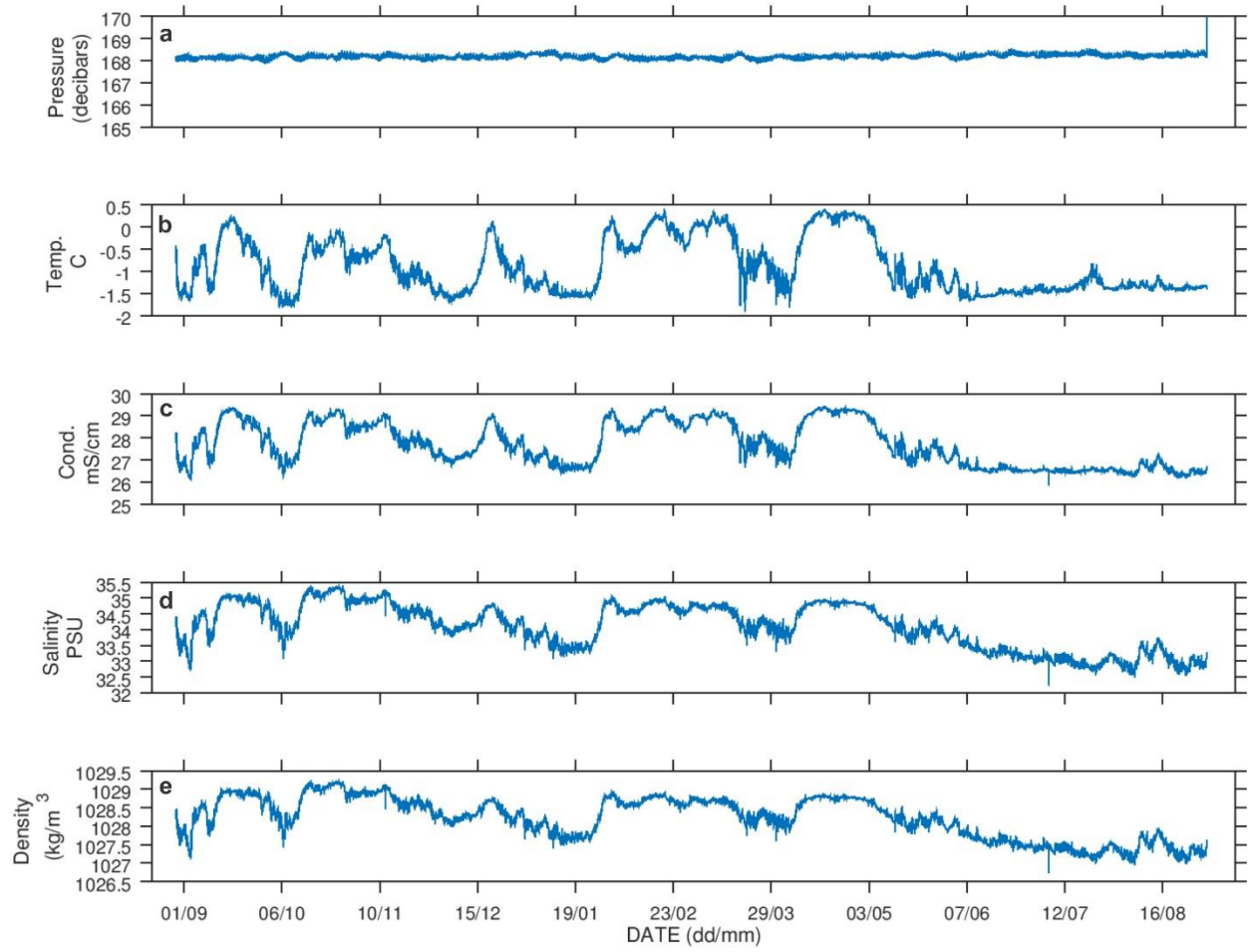
Figure 7 Time series of (a) pressure, (b) temperature, (c) conductivity, (d) salinity and (e) density from the Seabird CTD.
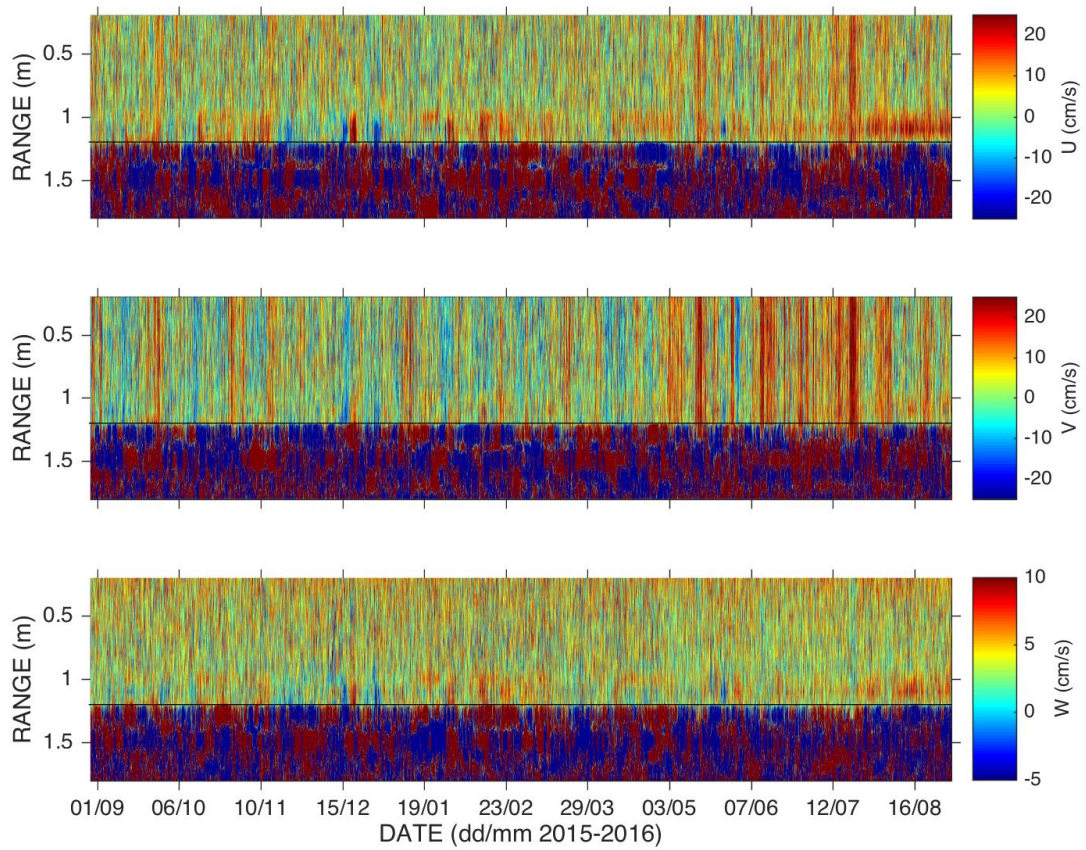
Figure 8 Time series of the vertical profiles of the three components of velocity. U component (east/west) (top panel), V component (north/south) (middle panel), W component (up/down) (bottom panel) as recoded by the Aquadopp ADCP. The y-axis represents the range distance away from the ADCP transducer. Velocity magnitude is given by the color scales to the right of each panel. Positive U, V and W are to the east, north, and downward respectively. Solid line demarcates the last good bin above bottom.
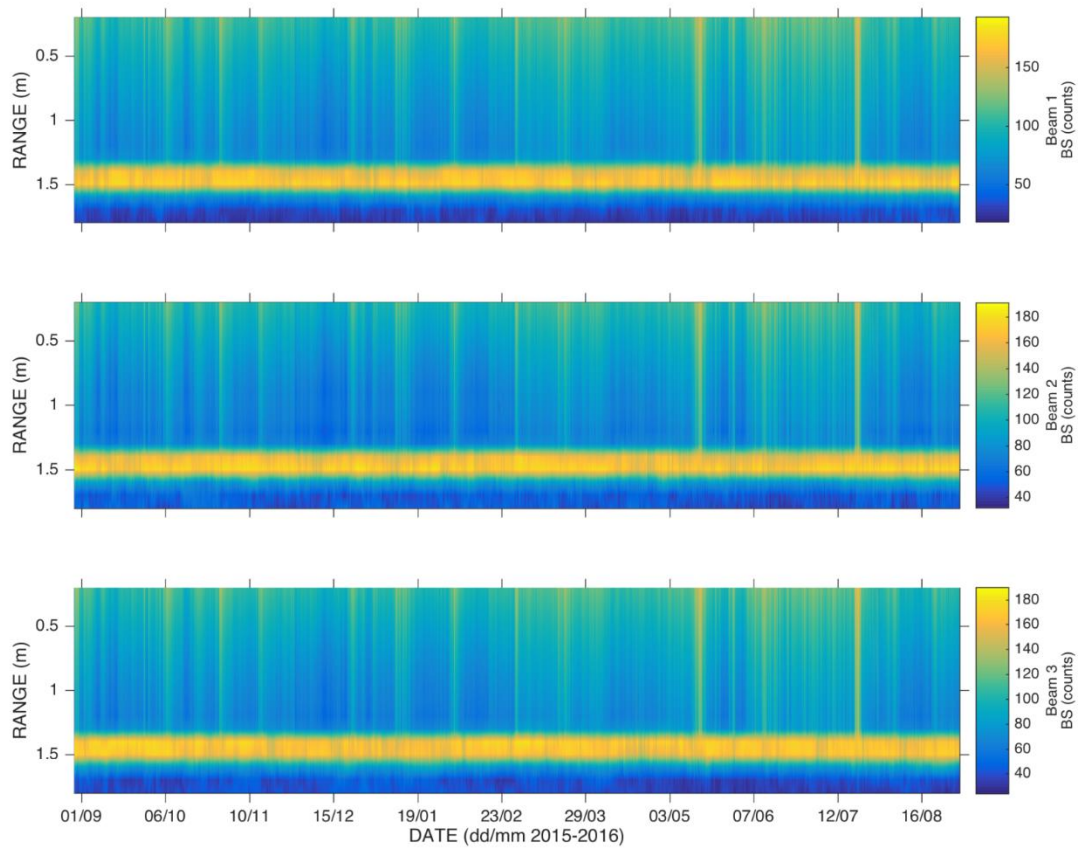
Figure 9 Time series of the vertical profiles of raw acoustic backscatter intensity (BS in counts) for beams 1 (top panel) through 3 (bottom panel) of the Aquadopp ADCP. The y-axis represents the range distance away from the ADCP transducer. The magnitude of the raw backscatter intensity in counts are shown by the colour scales to the right of each panel.
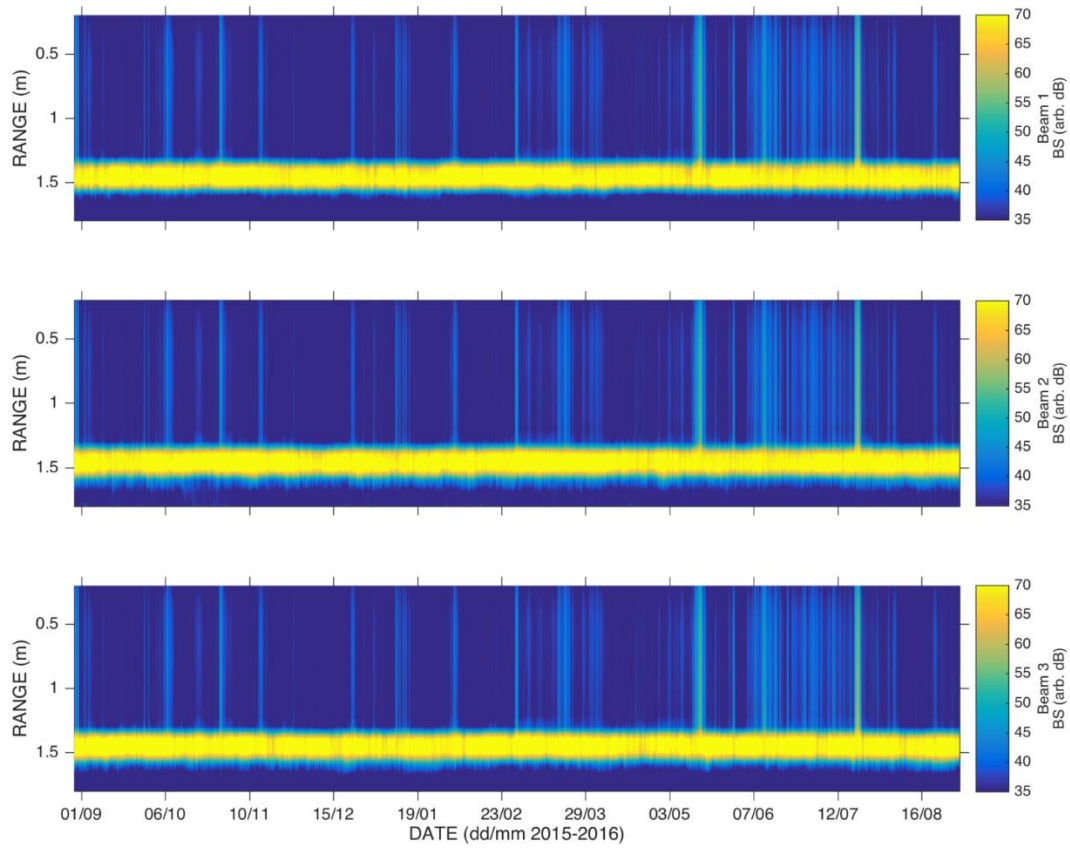
Figure 10 Time series of the vertical profiles of processed acoustic backscatter intensity for beams 1 (top panel) through 3 (bottom panel) of the Aquadopp ADCP. The y-axis represents the range distance away from the ADCP sonar. The backscatter intensity was converted from counts to arbitrary decibels (arb. dB) and slant-range corrected to account for spherical spreading and attenuation losses along the path. The magnitude of the corrected backscatter intensity is shown by the colour scales to the right of each panel.
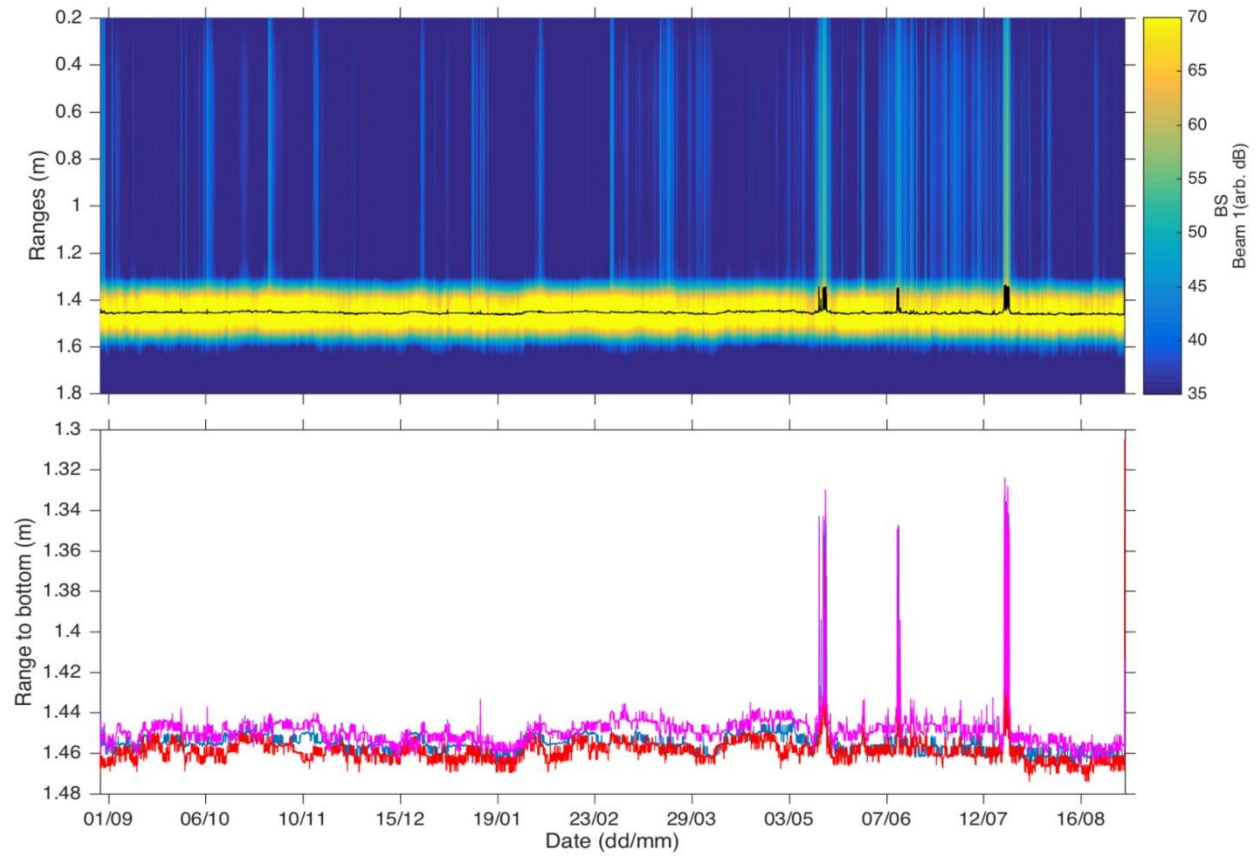
Figure 11 Vertical profile of corrected acoustic backscatter intensity for beam 1 of the Aquadopp ADCP (top panel) and the distance to the bottom (bottom panel) determined using the backscatter profile of beam 1 (blue), beam 2 (red) and beam 3 (pink).
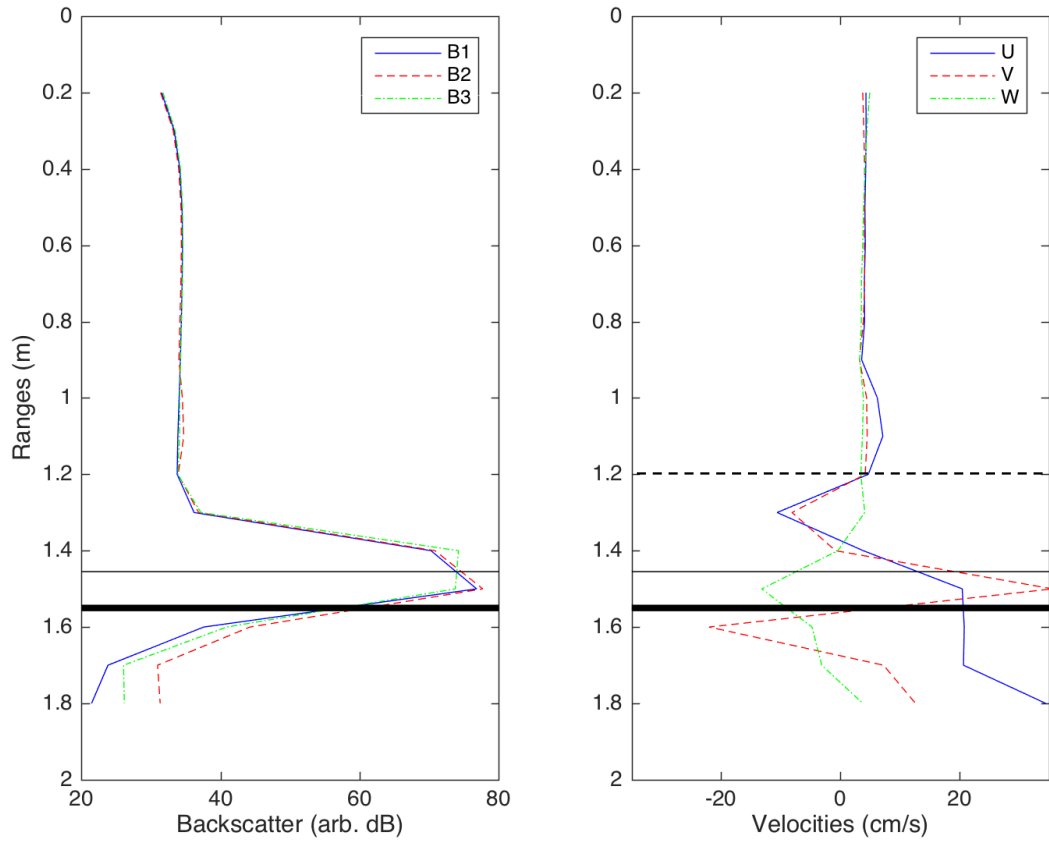
Figure 12 Mean profiles over deployment duration of corrected backscatter (left) and velocity component (right). Profiles of mean corrected backscatter intensities are shown for beams 1 (blue), 2 (red) and 3 (green). Profiles of mean velocity components are shown for U (blue), V (red) and W (solid green). The y-axis represents the range distance away from the ADCP transducer. The log-book value of the height of ADCP above ground (HAB = 155cm) is indicated by the thick solid black line, while the distance measured acoustically is shown by the thin black line. The last good bin for velocity is indicated by the dashed black line (bin 11, 1.2 m range) in the right panel.
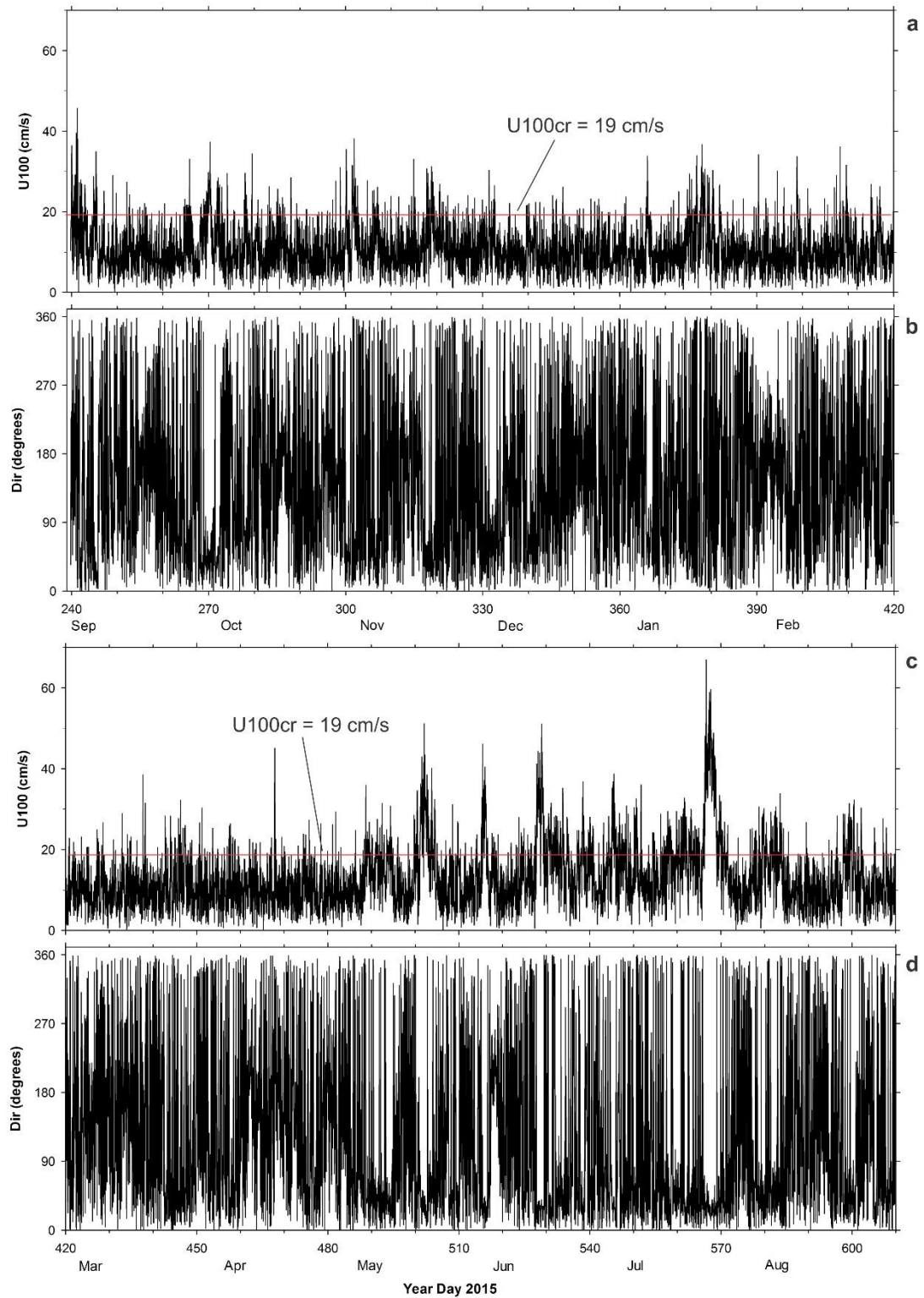
Figure 13 Time series of mean current speed at 1 m above bottom, U100, and the direction of U100 recorded by the Aquadopp ADCP. (a) and (b) for year-day 240 – 420. (c) and (d) for year-day 420 – 610. The redlines represent the threshold current speed U100cr of 19 cm/s for bedload transport for muddy sediments in the Beaufort Sea.

34
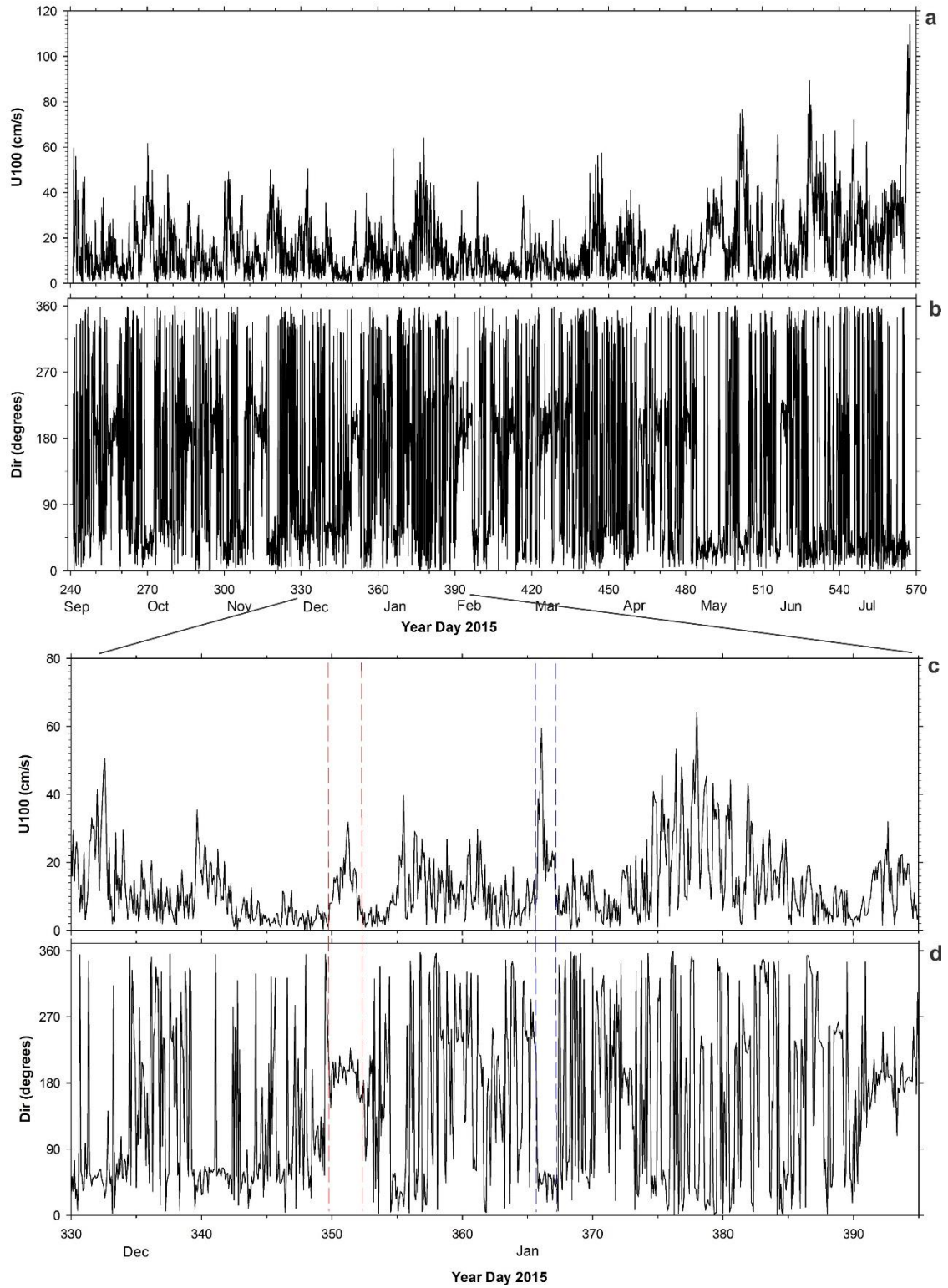
Figure 14 Time series of mean current speed U100 and current direction recorded by the MAVS. Panels a, b are for the entire duration and Panels c, d for the period December 2015 to January 2016. The pairs of blue and red dashed lines in (c, d) respectively demarcate a current event with currents to the northeast and another event with currents to the south-southwest.
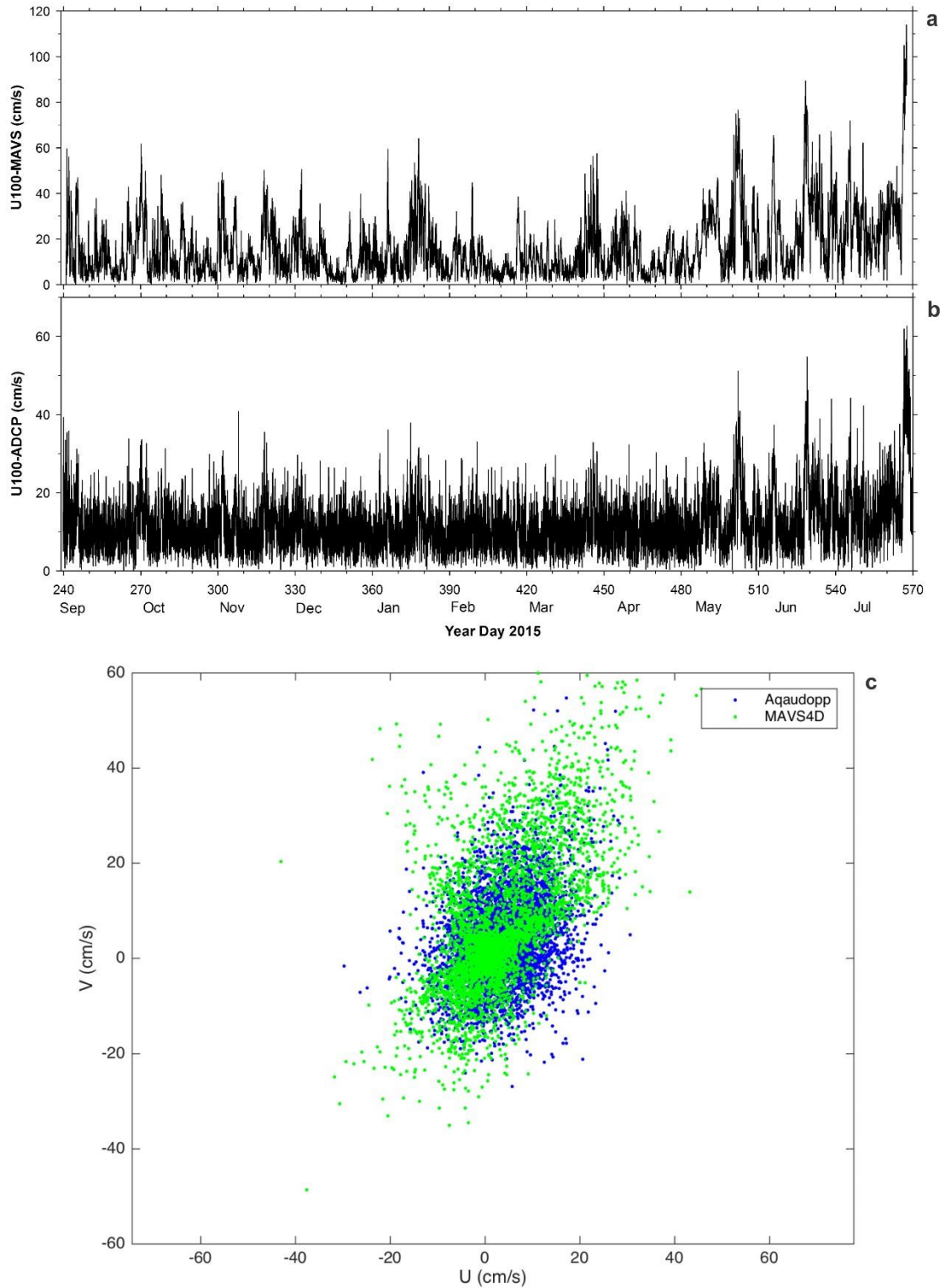
Figure 15 Comparison of bottom currents from the MAVS and the ADCP. Panels (a) and (b) are the time series of U100 recorded by MAVS and the ADCP for the period September 1 2015 to July 20 2016. Panel (c) is the scatter plot of the U and V components at 100 cmab measured by MAVS (in green) and ADCP (in blue).

36
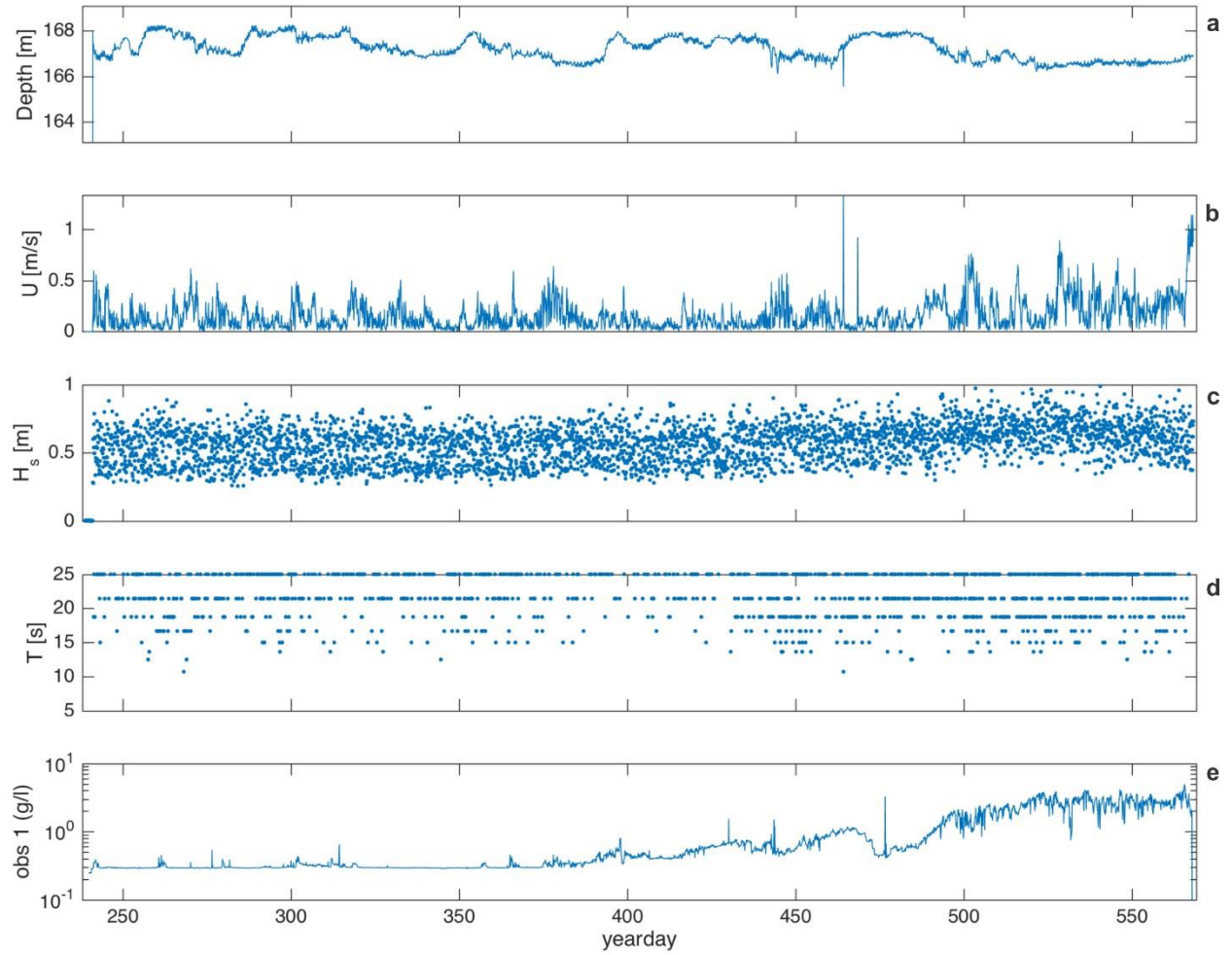
Figure 16 Time series of (a) depth, (b) mean speed U (100 cmab), (c) significant wave height Hs, (d) peak wave period T and (e) despiked mean sediment concentration OBS1 (1 mab) from the MAVS4D.
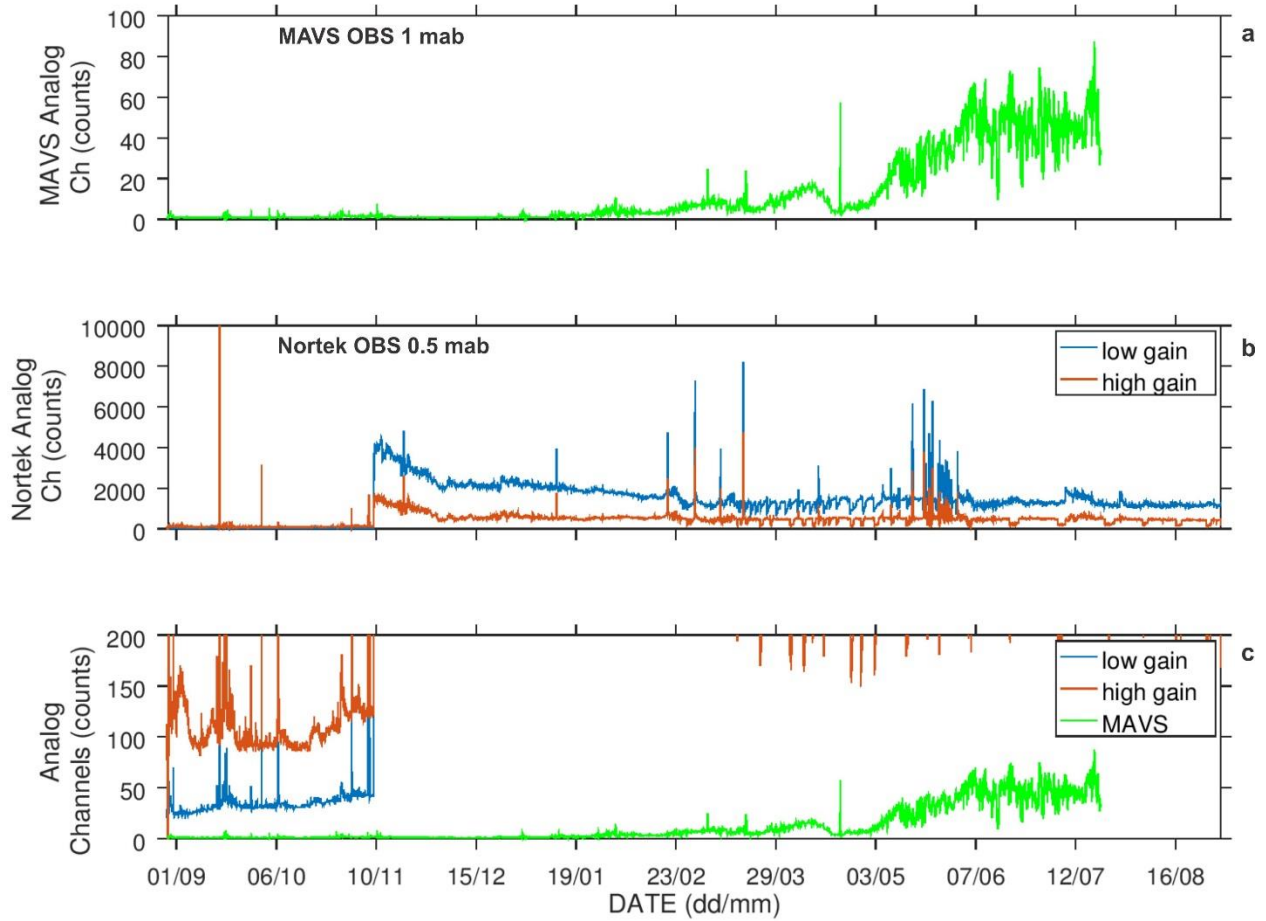
Figure 17 Time series of analog count values from (a) MAVS OBS at 1 mab (green), (b) the OBS connected to the Nortek ADCP at 0.5 mab in low gain (blue) and high gain (red) settings, and (c) all three analog channels plotted over a range of 0 to 200 counts.
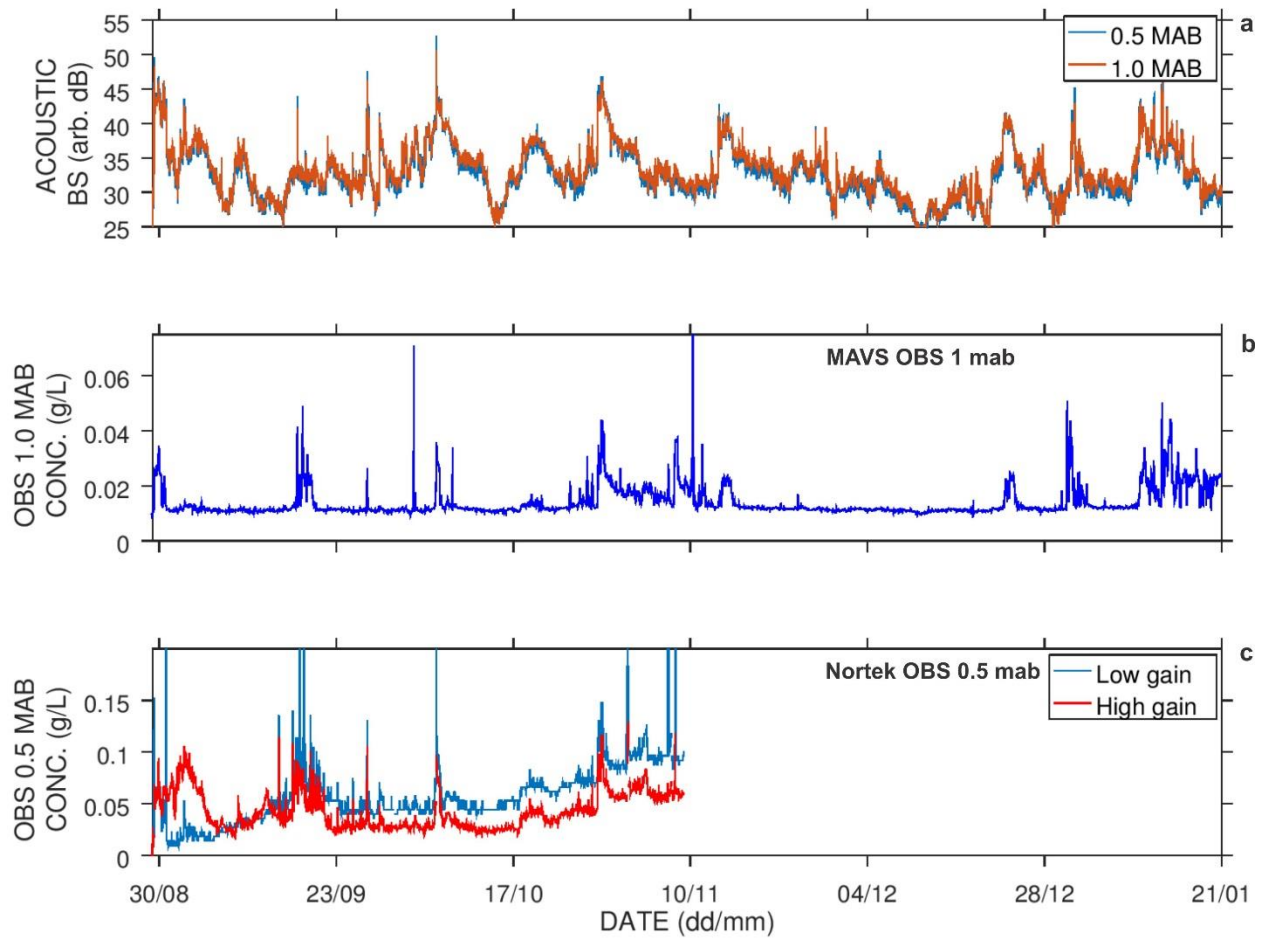
Figure 18 Temporal variations of (a) corrected acoustic backscatter from beam 1 of the ADCP at 0.5 mab (blue) and 1 mab (orange) and converted suspended sediment concentration (SSC) from (b) the MAVS OBS at 1 mab and (c) the ADCP OBS at 0.5 mab at low gain (blue) and high gain (red) for the time period of 29 August to 21 January.
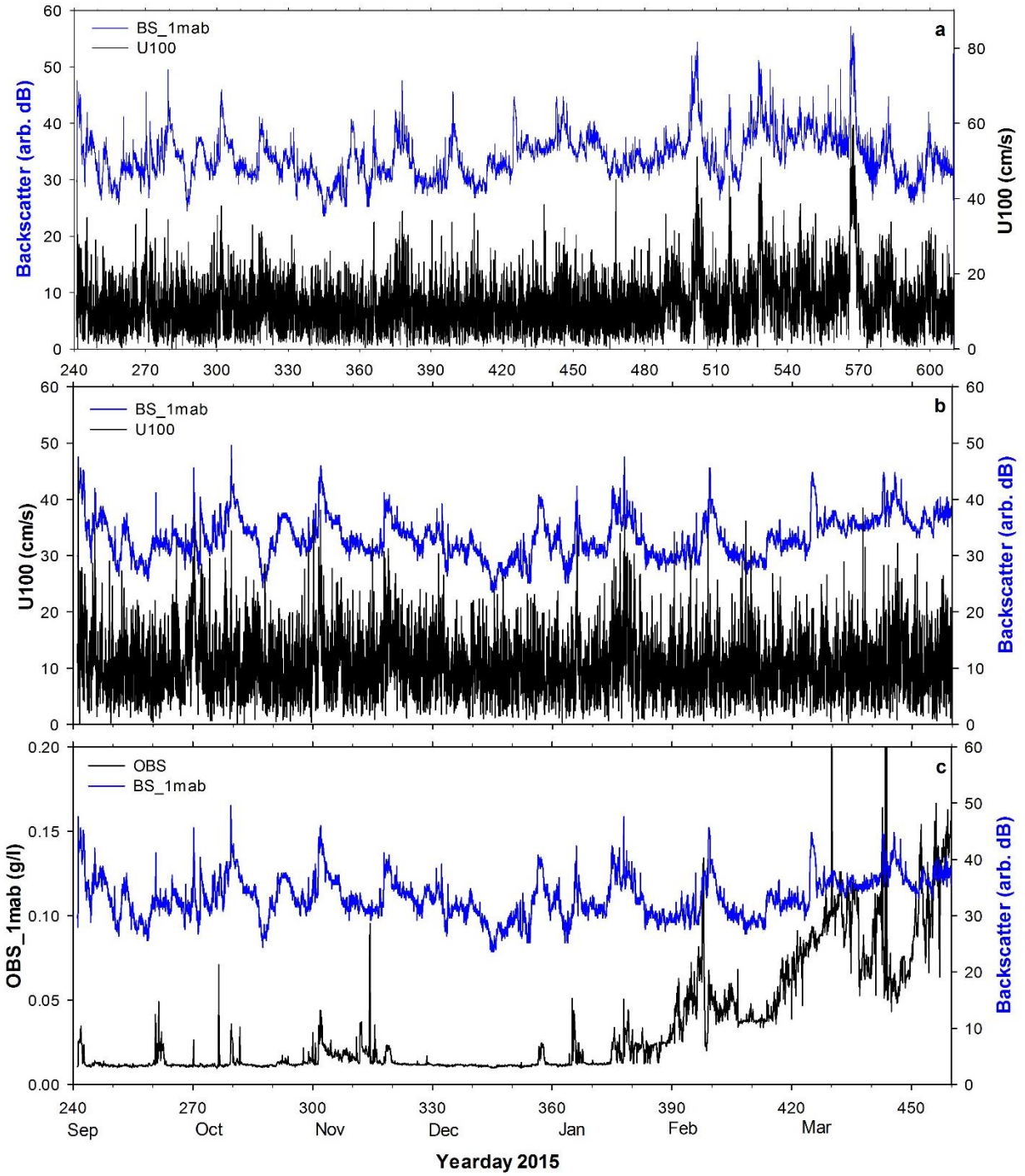
Figure 19 Panel (a) compares the temporal variation of backscatter intensity and the current speed U100 recorded by the ADCP for the entire deployment duration. Panels (b) and (c) are the temporal variations of U100, backscatter intensity, and the SSC from the MAVS OBS at 1 mab for the select period of yearday 240 – 460 (September 2015 – March 2016).

40
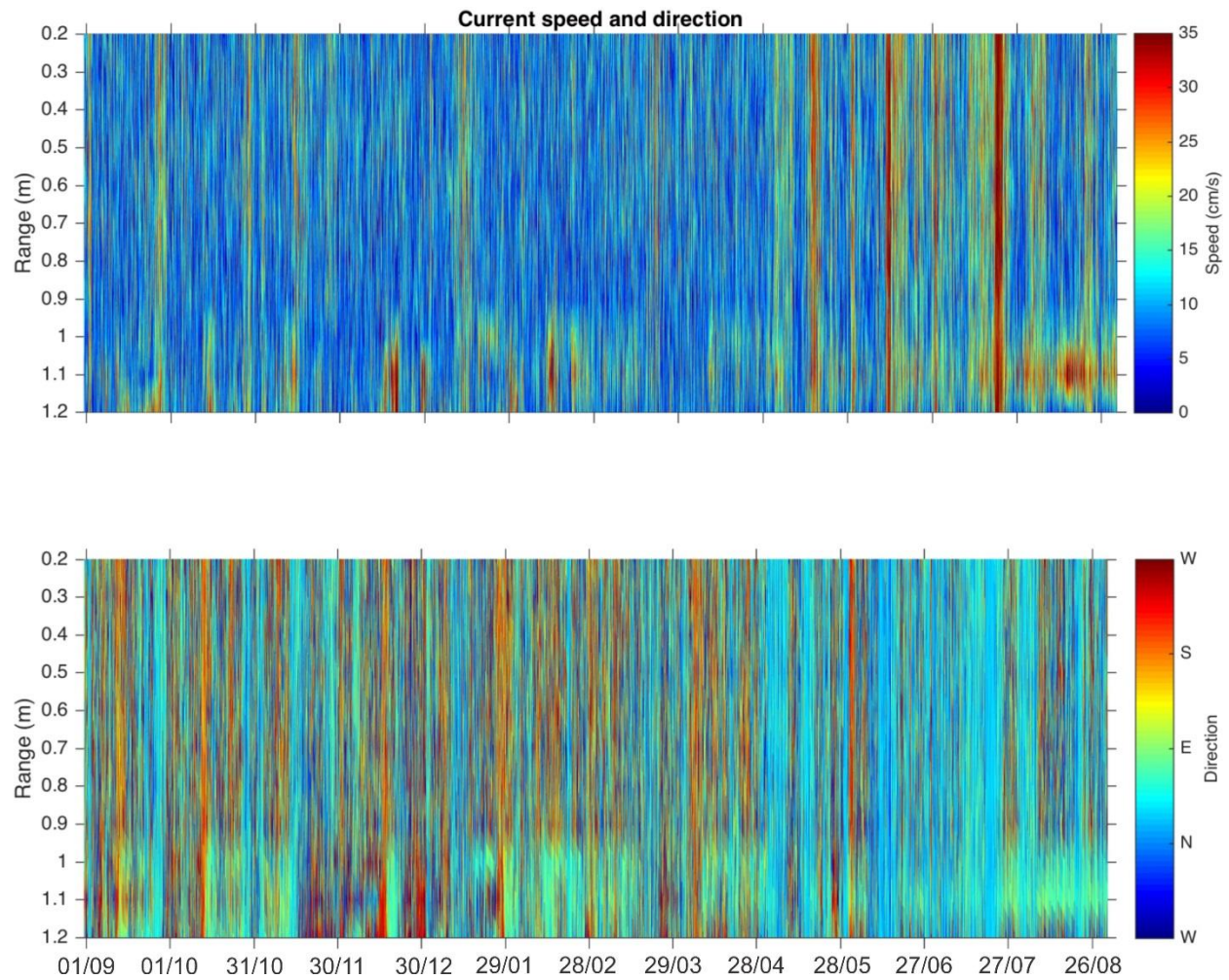
Figure 20 Current speed (top) and direction (bottom) as measured by the Aquadopp ADCP. Range from the transducer is indicated on the y-axis and time on the x-axis. Current speed (cm/s) and direction (compass, direction to) are represented by the respective color legends.
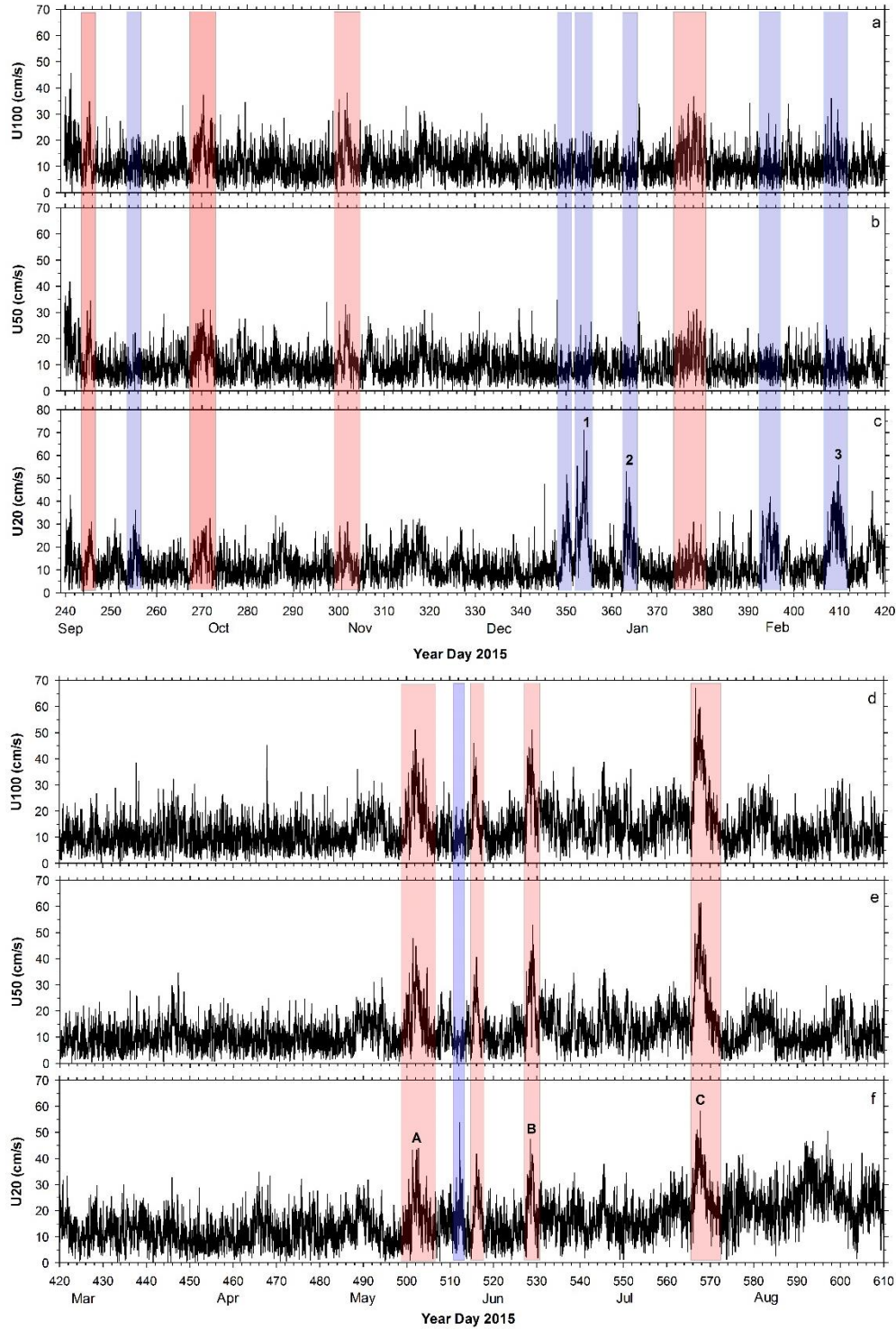
Figure 21 Time series of current speed at 1, 0.5 and 0.2 mab from the ADCP. Panels (a-c) for the period yearday 240-420 and Panels (d-f) for the period yearday 420-610. More significant Type ii and iii events are respectively highlighted with red and blue color bars. The selected Type iii events 1-3 and Type ii events A-C presented in Figure 22 and discussed in details are also labeled.
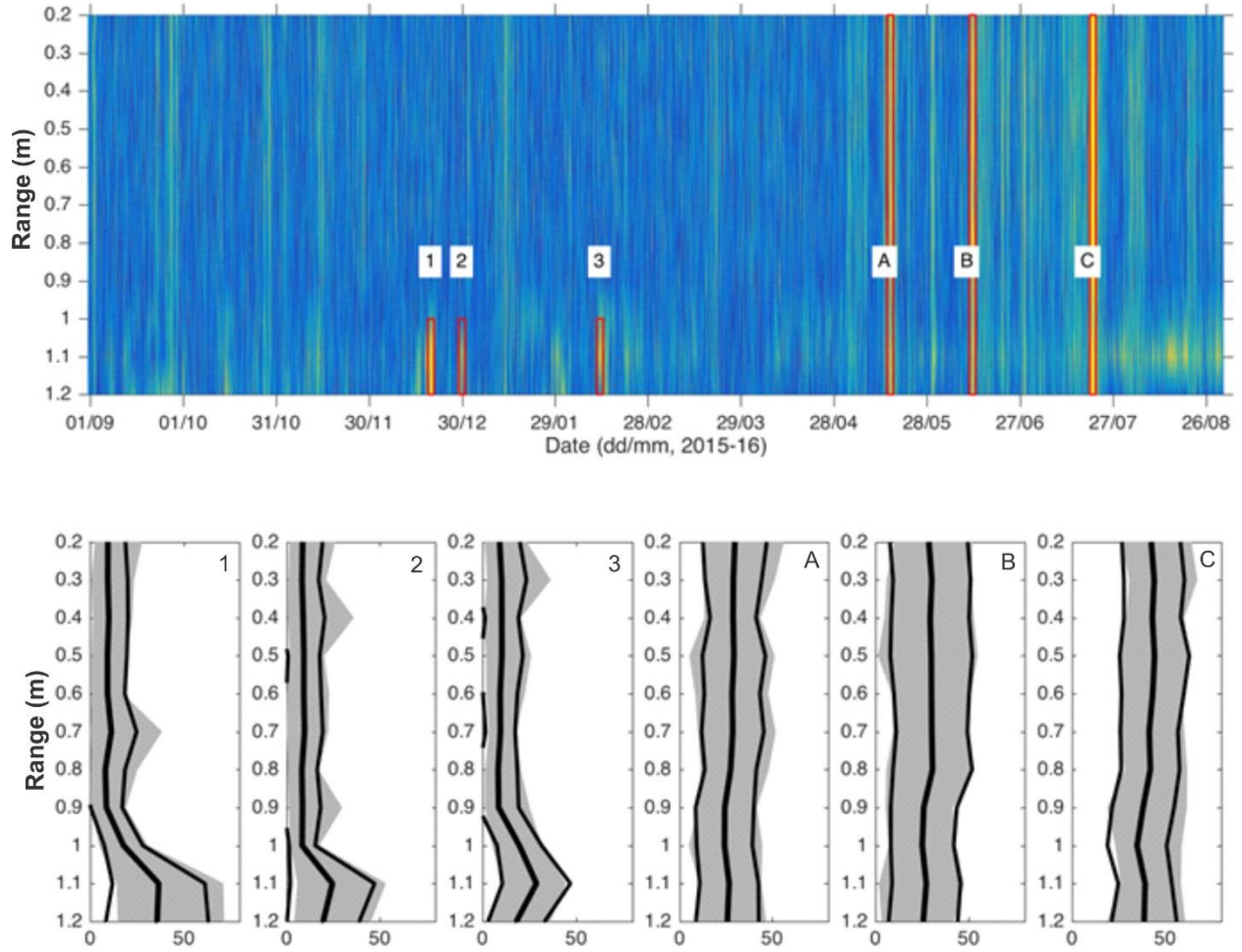
Figure 22 Top panel presents the vertical profiles of current speed recorded by the ADCP as a function of time (x-axis) and range in m from the Aquadopp transducer (y-axis). Selected Type iii events (1-3) and Type ii events (A-C) were labeled and marked by red rectangles. Current magnitudes are shown by the intensity of the yellow color. Bottom panels show speed profiles (cm/s) for events 1-3 (left) and A-C (right) with the range of all velocities marked by the shaded region, mean velocity profiles over the 48 hour window shown in solid black, and +/-1 standard deviation shown in thin black lines.
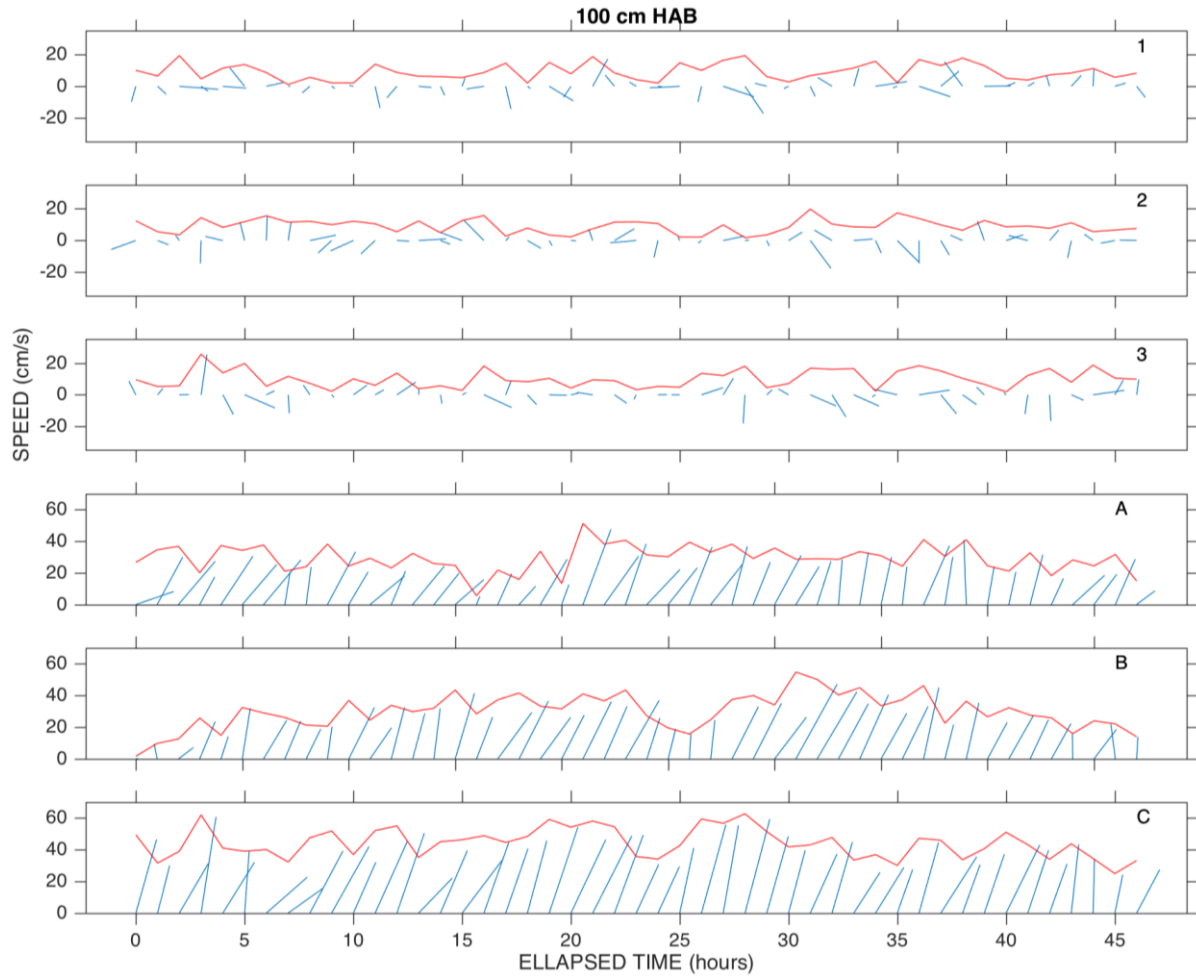
Figure 23 Speed magnitude (in red) and vectors (in blue) at 1 mab over 48 hour windows for selected Type iii events 1-3 (top three panels) and Type ii events A-C (bottom three panels).
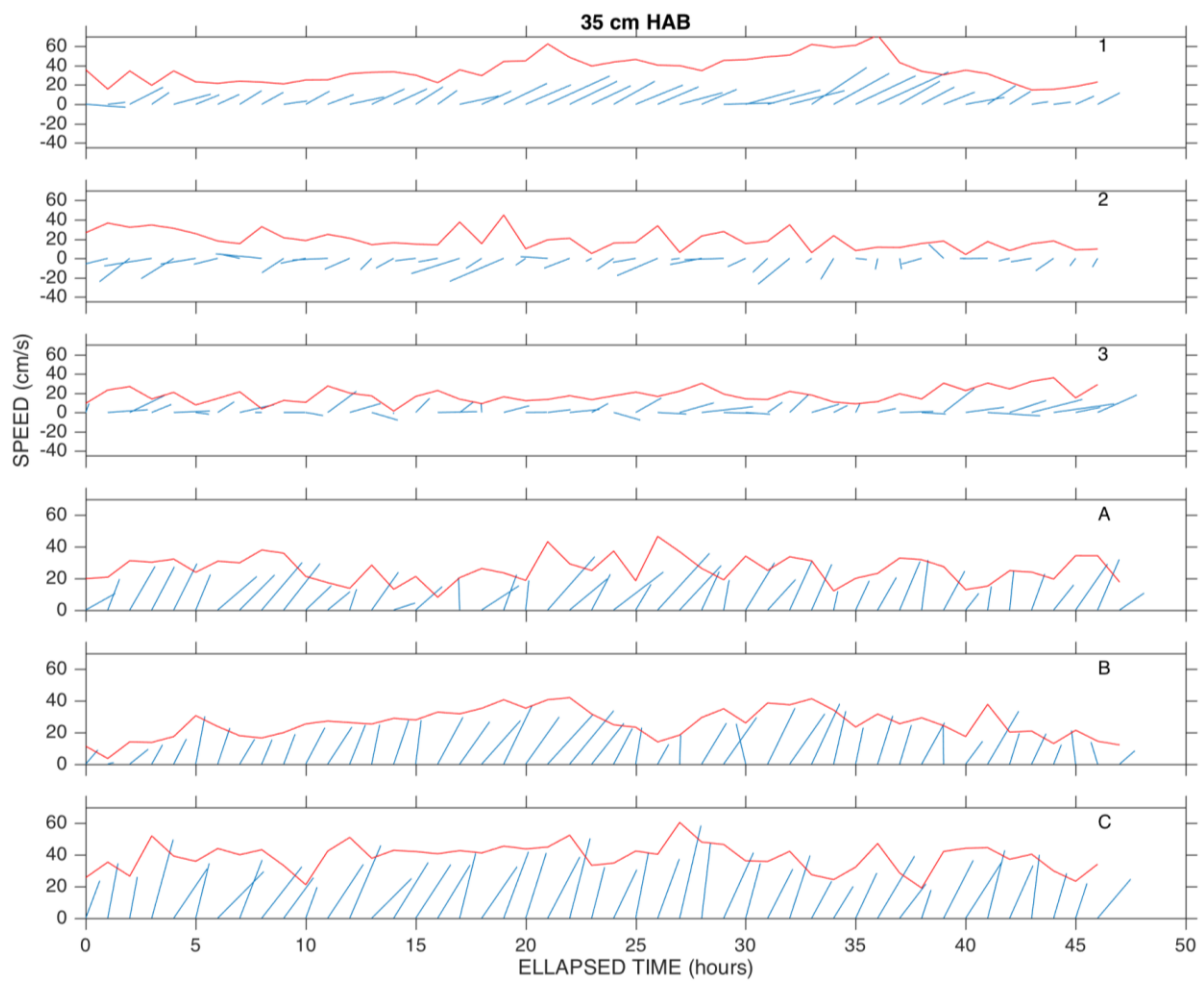
Figure 24 Same as that of Figure 23 but at 0.35 mab.
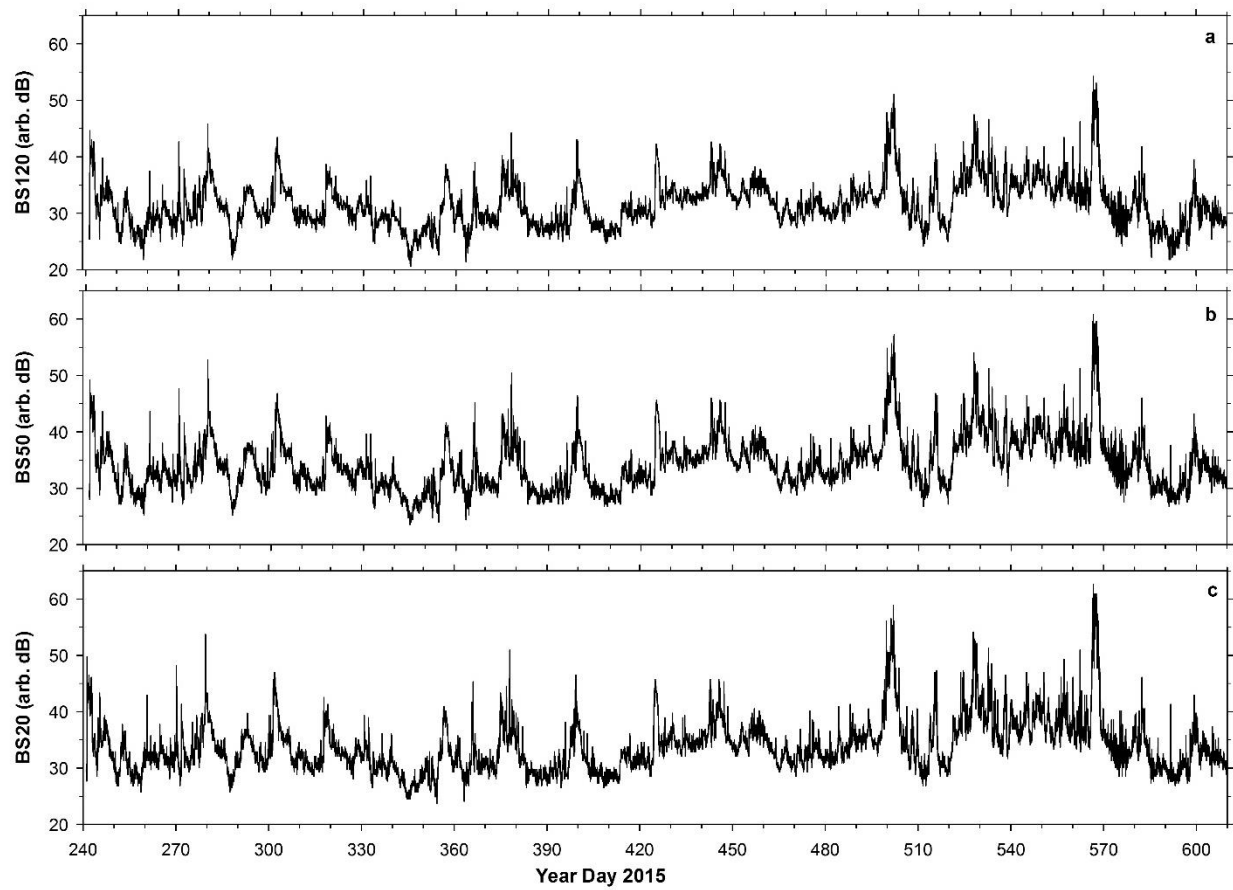
Figure 25 Temporal variations of the corrected backscatter intensity (BS in arb. dB) at (a) 1.2, (b) 0.5 and (c) 0.2 mab from the ADCP.
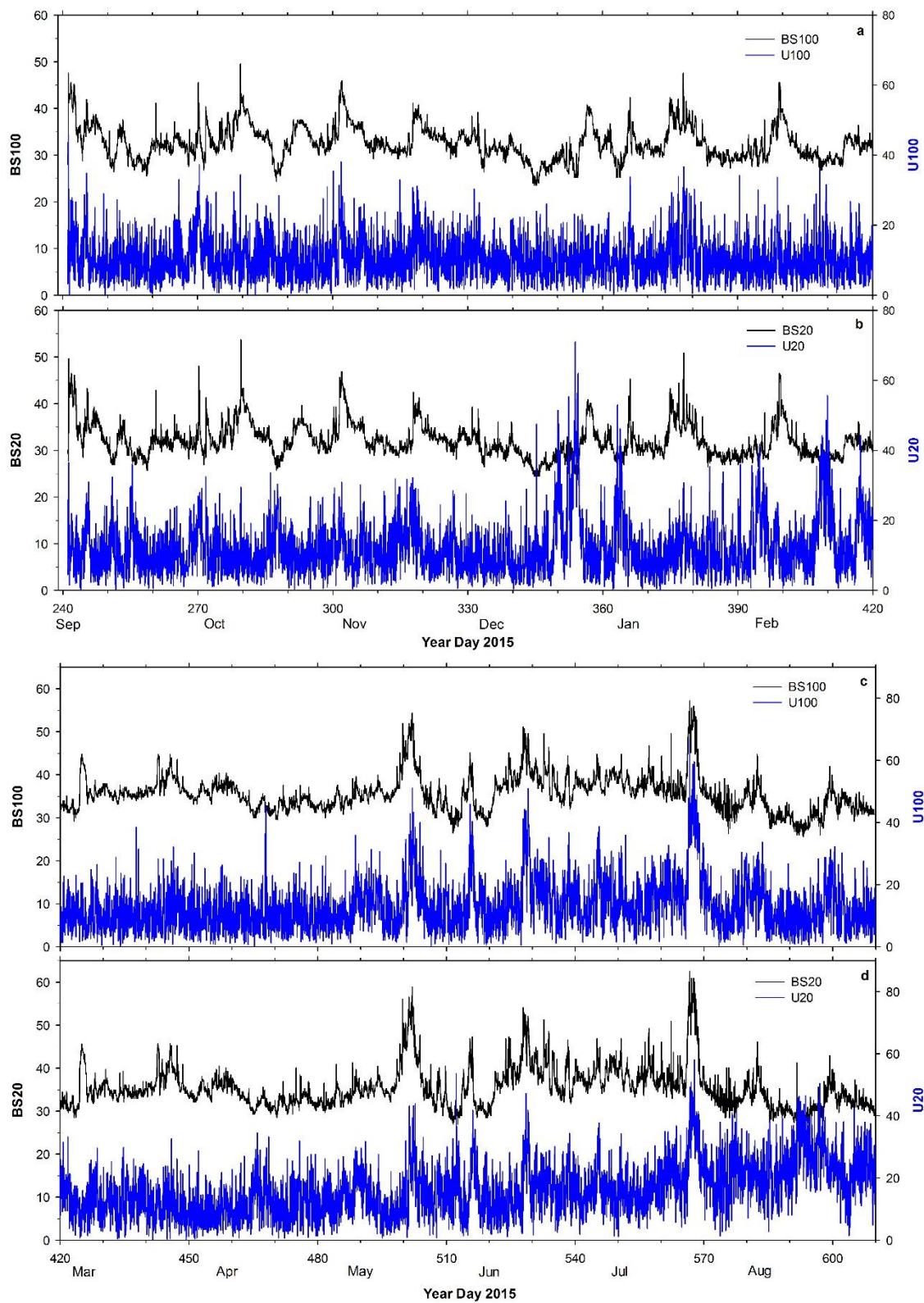
Figure 26 Time series of backscatter intensity at 0.2 (BS20) and 1 (BS100) mab in comparison with current speed (U20, U100) for (a, b) yearday 240 – 420 and (c, d) yearday 420 – 610.

47
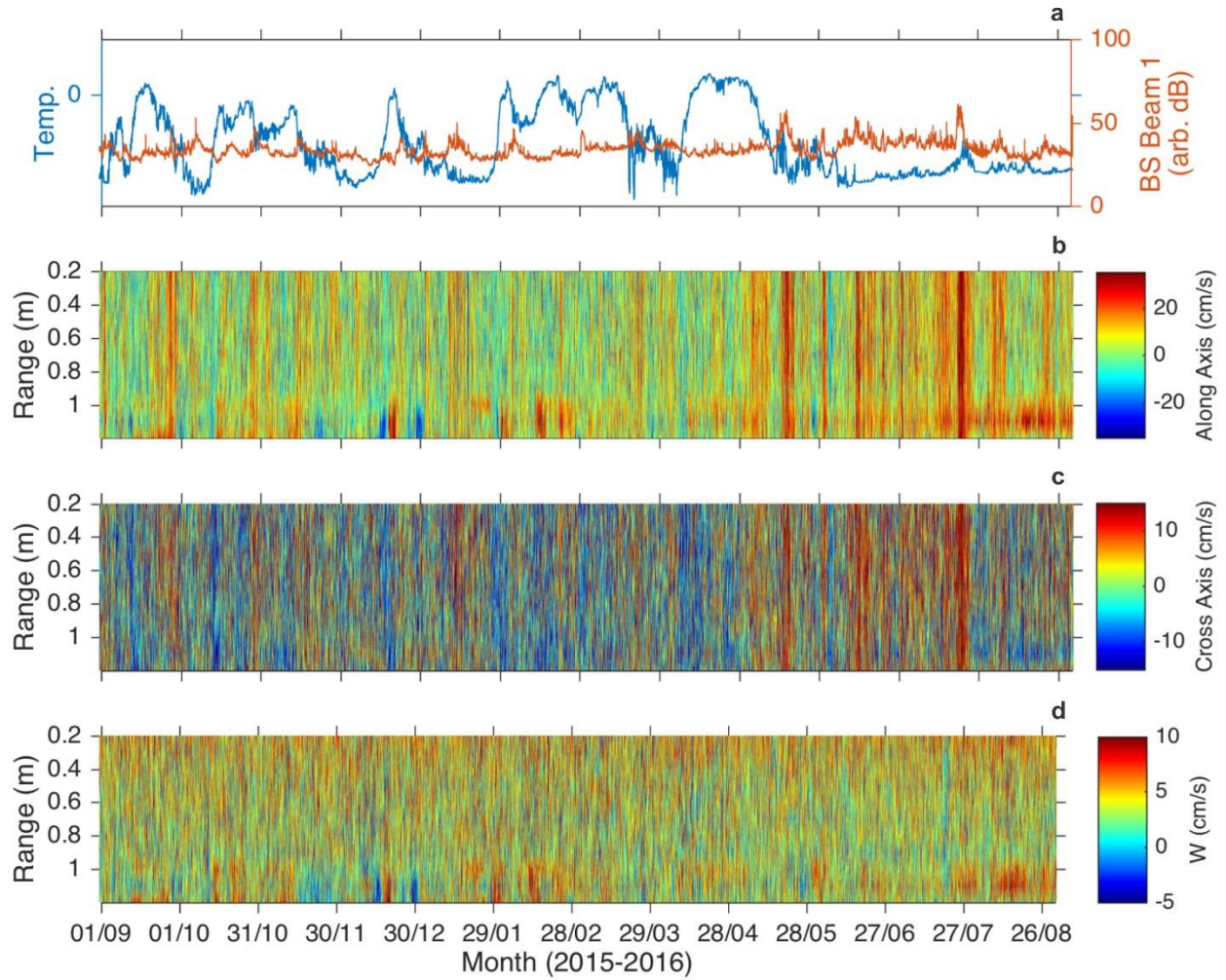
Figure 27 Temporal variations of (a) temperature (blue) and backscatter intensity (beam 1; orange), the vertical profiles of the rotated (b) along-shelf and (c) cross-shelf velocity components and (d) vertical velocity for the entire deployment duration. Positive values mean respectively down-shelf to the NE, offshore to the NW and downward for the along-shelf, cross-shelf, and vertical velocity components.
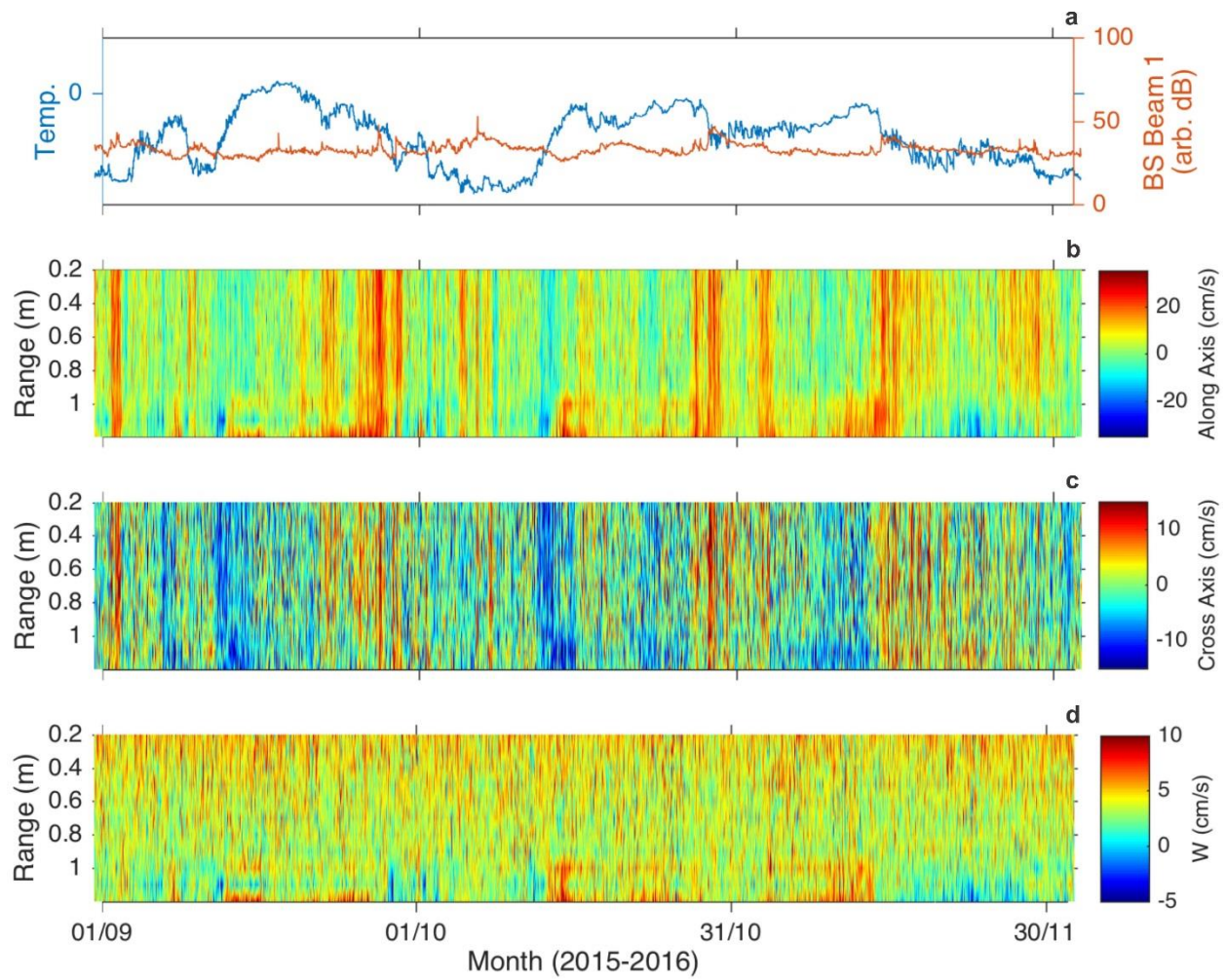
Figures 28 The same as Figure 27 but for the 3-month periods of September – November.
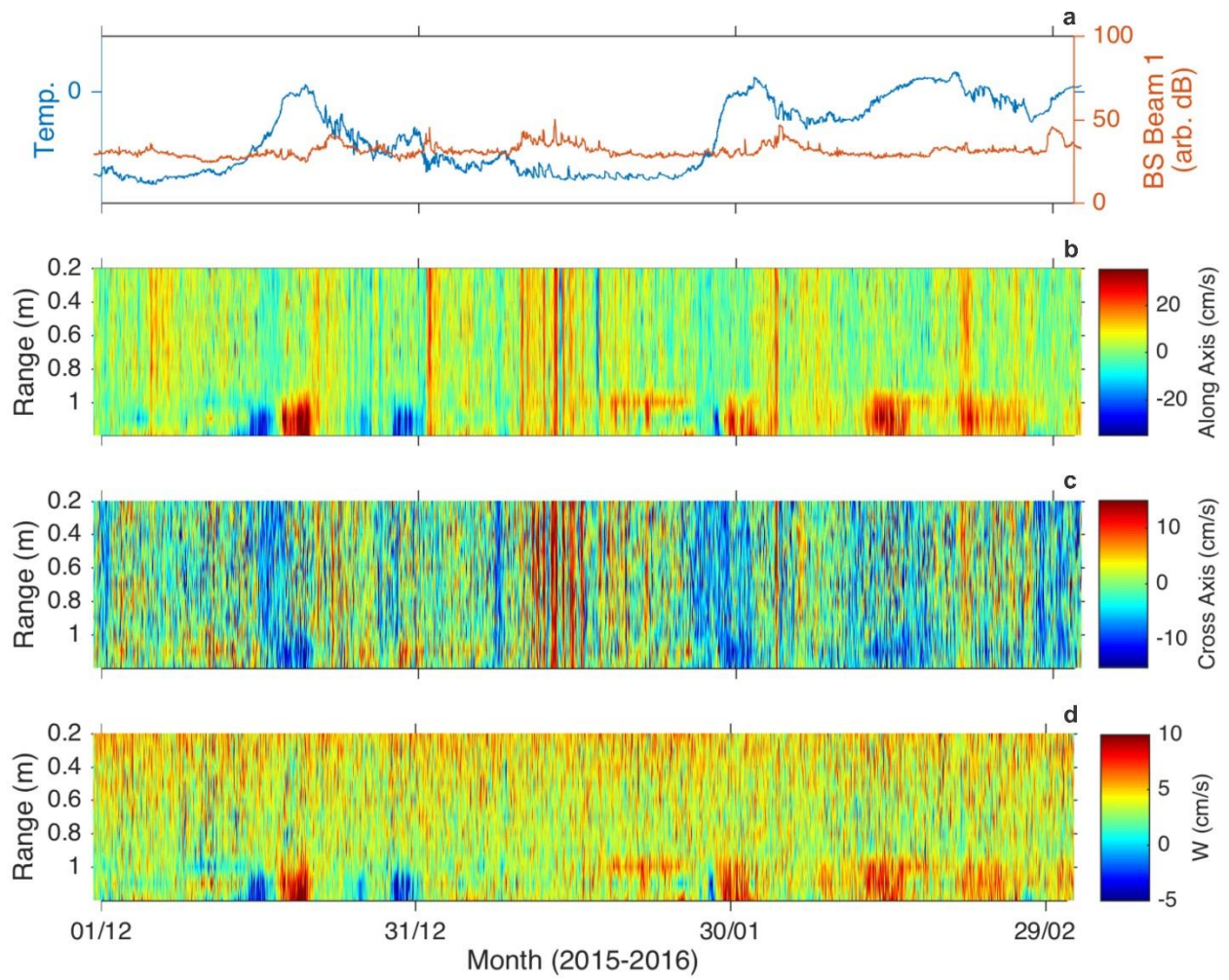
Figures 29 The same as Figure 27 but for the 3-month periods of December – February.
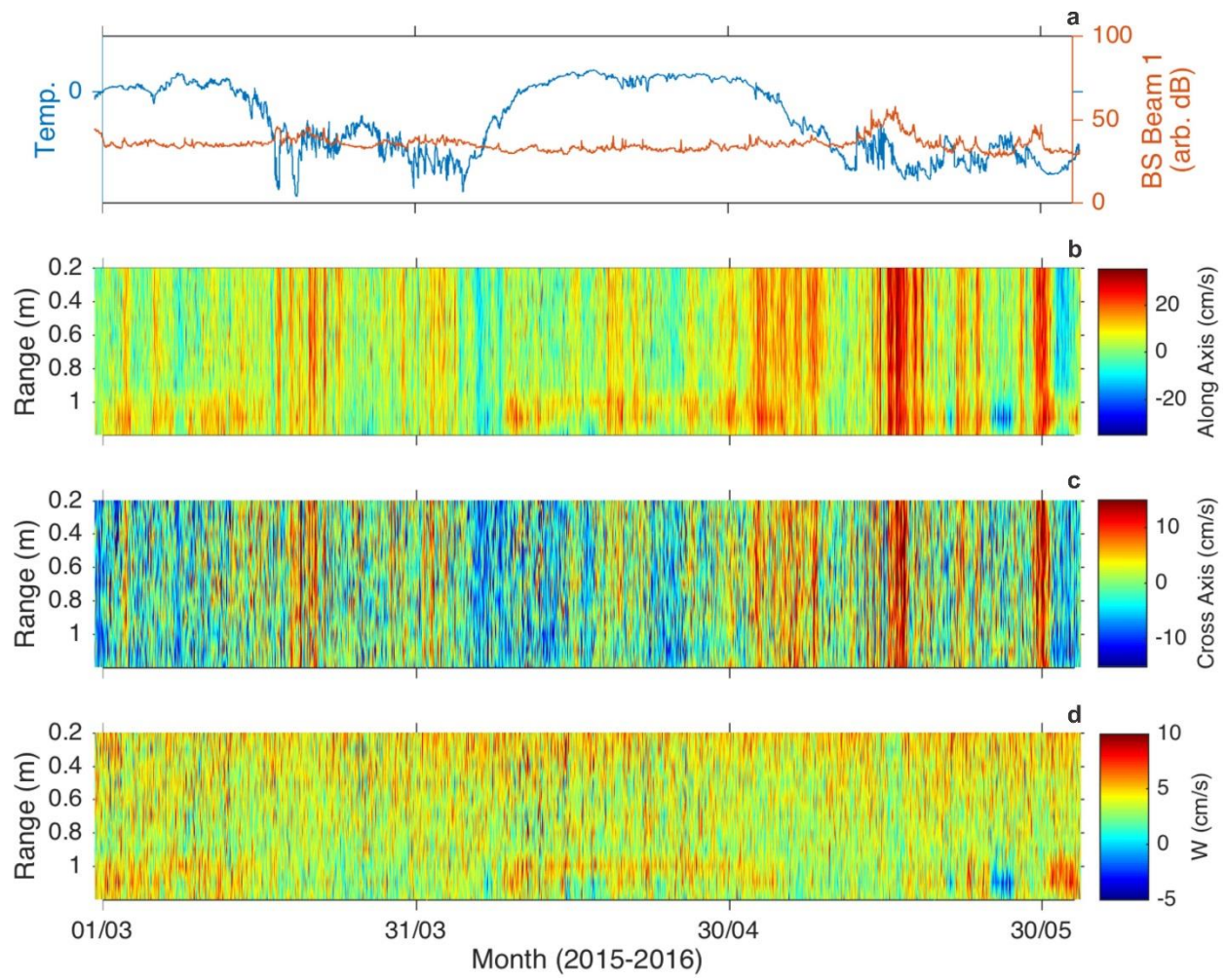
Figures 30 The same as Figure 27 but for the 3-month periods of March – May.
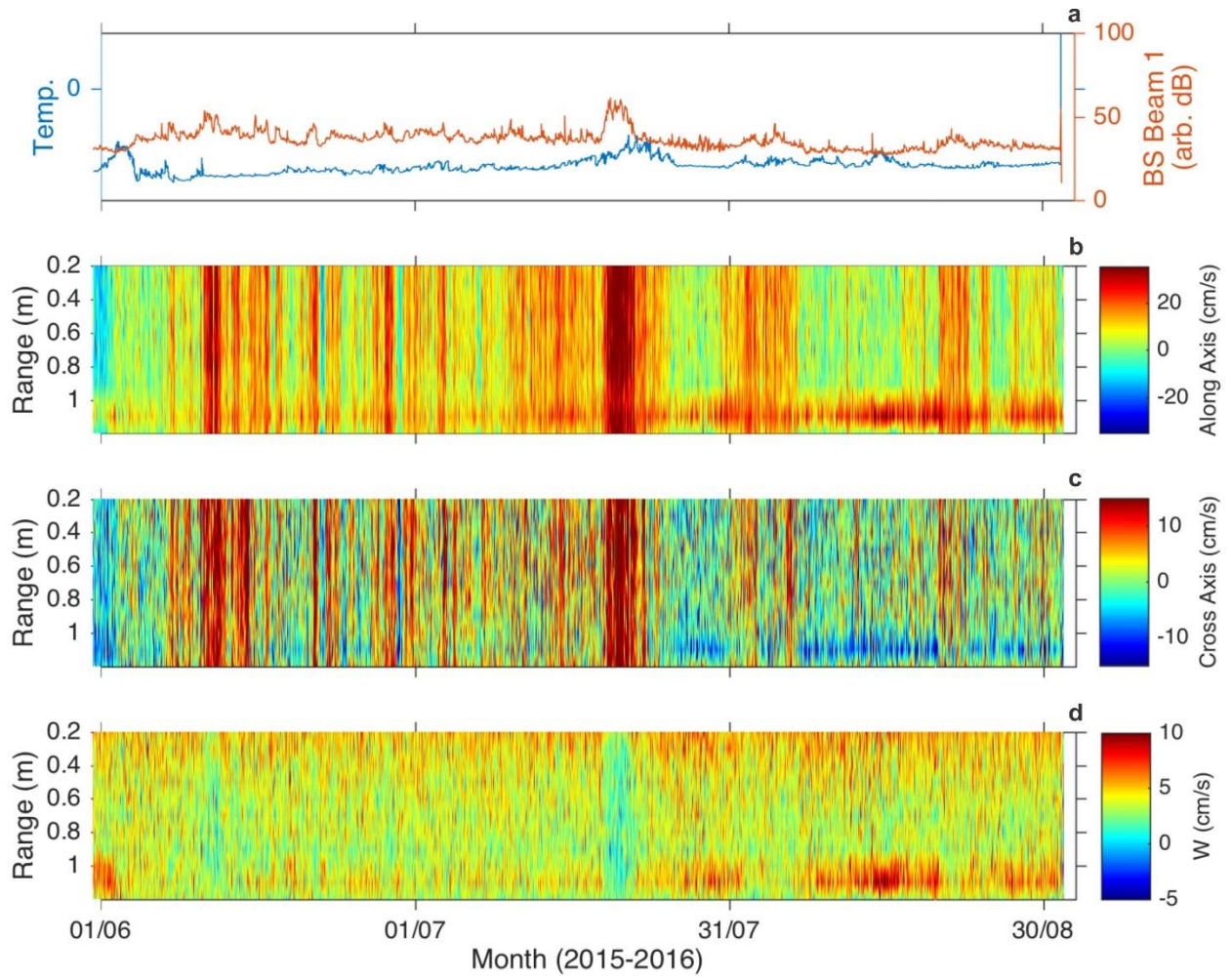
Figures 31 The same as Figure 27 but for the 3-month periods of June – August.
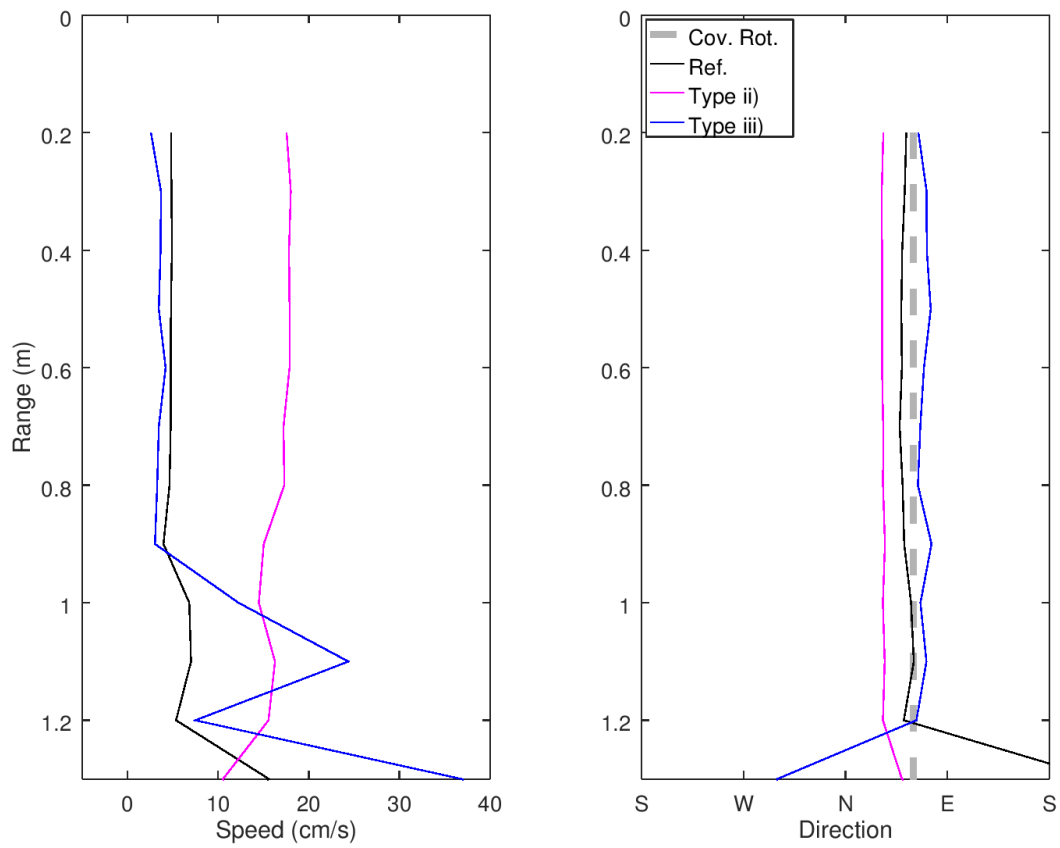
Figure 32 Mean profiles of current speed (left) and direction (right) for time defined as Type ii events (magenta), time defined as Type iii events (blue), and all other times not defined as either Type ii or Type iii events (Ref in black). Y axes are range distance from the ADCP transducer.
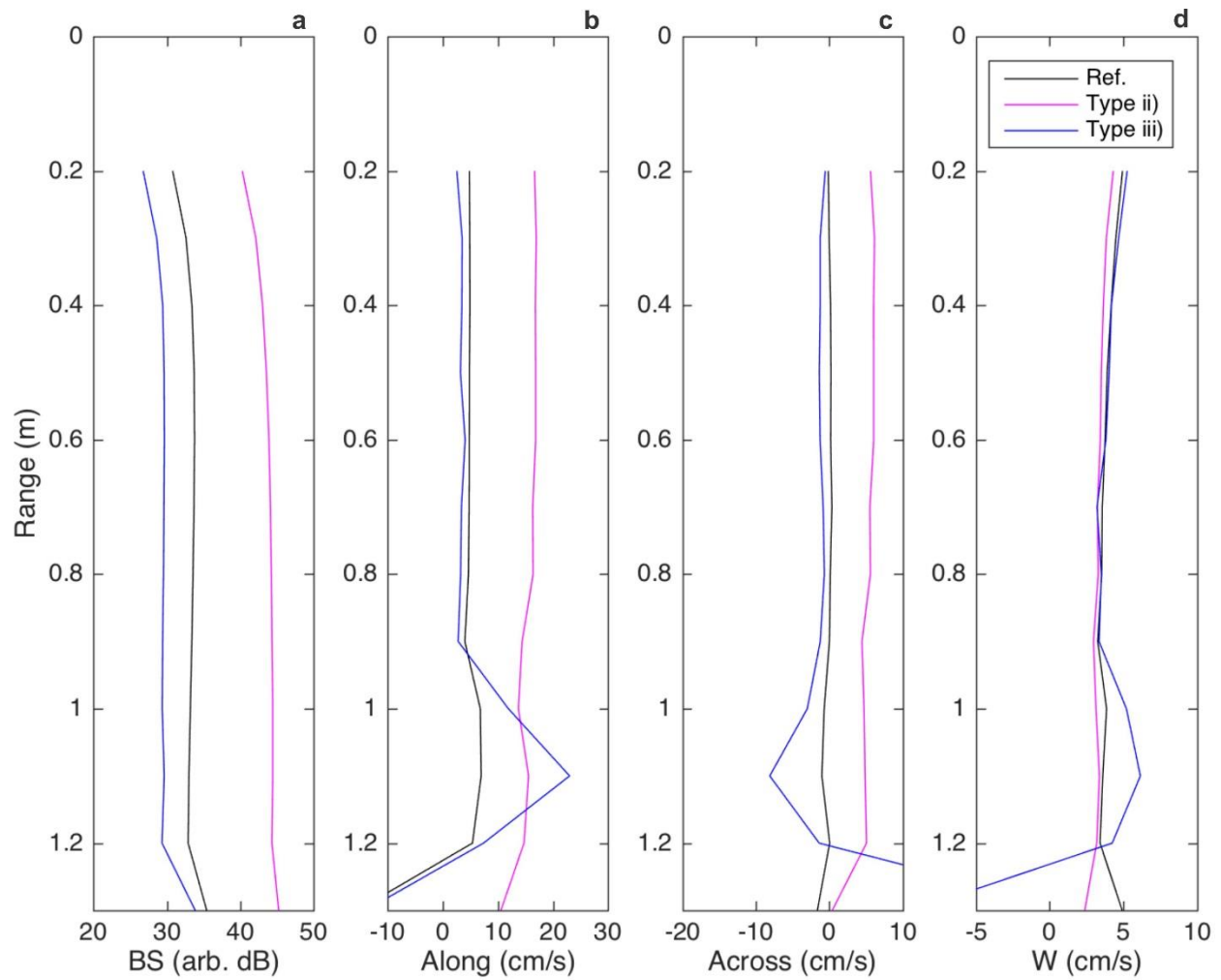
Figure 33 Mean profiles of (a) backscatter intensity from beam 1, (b) along-shelf, (c) across-shelf and (d) vertical velocity components W averaged for time defined as Type ii events (magenta), time defined as Type iii events (blue), and all other times not defined as either Type ii or Type iii events (Ref in black). Y axes are range distance from the ADCP transducer.
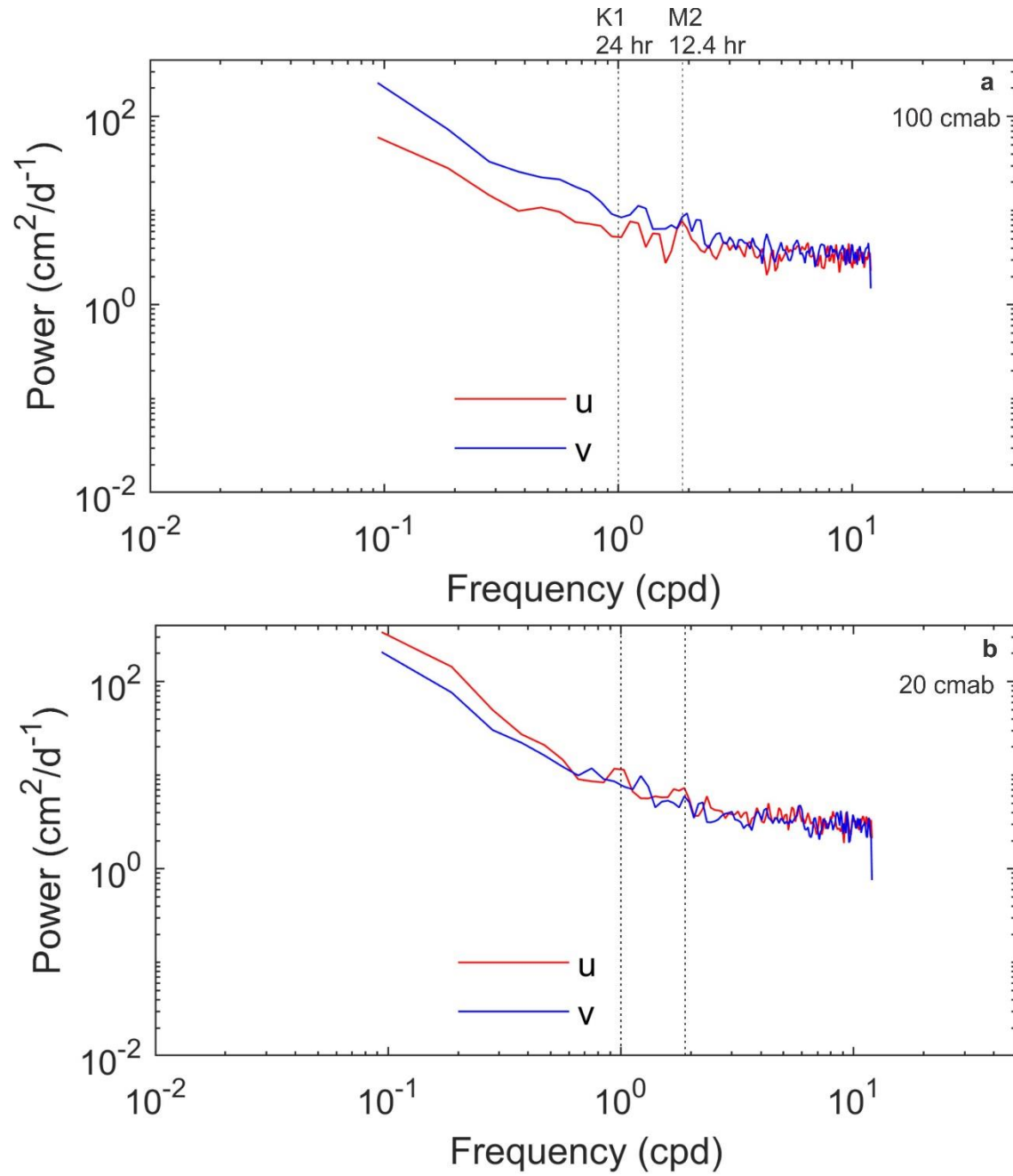
Figure 34 Spectral power versus frequency for the u and v velocity components measured at (a) 100 cm above bottom and (b) 20 cmab. Vertical dashed lines demark respectively M2 (12.4 hr) and K1 (24 hr) tidal frequencies.
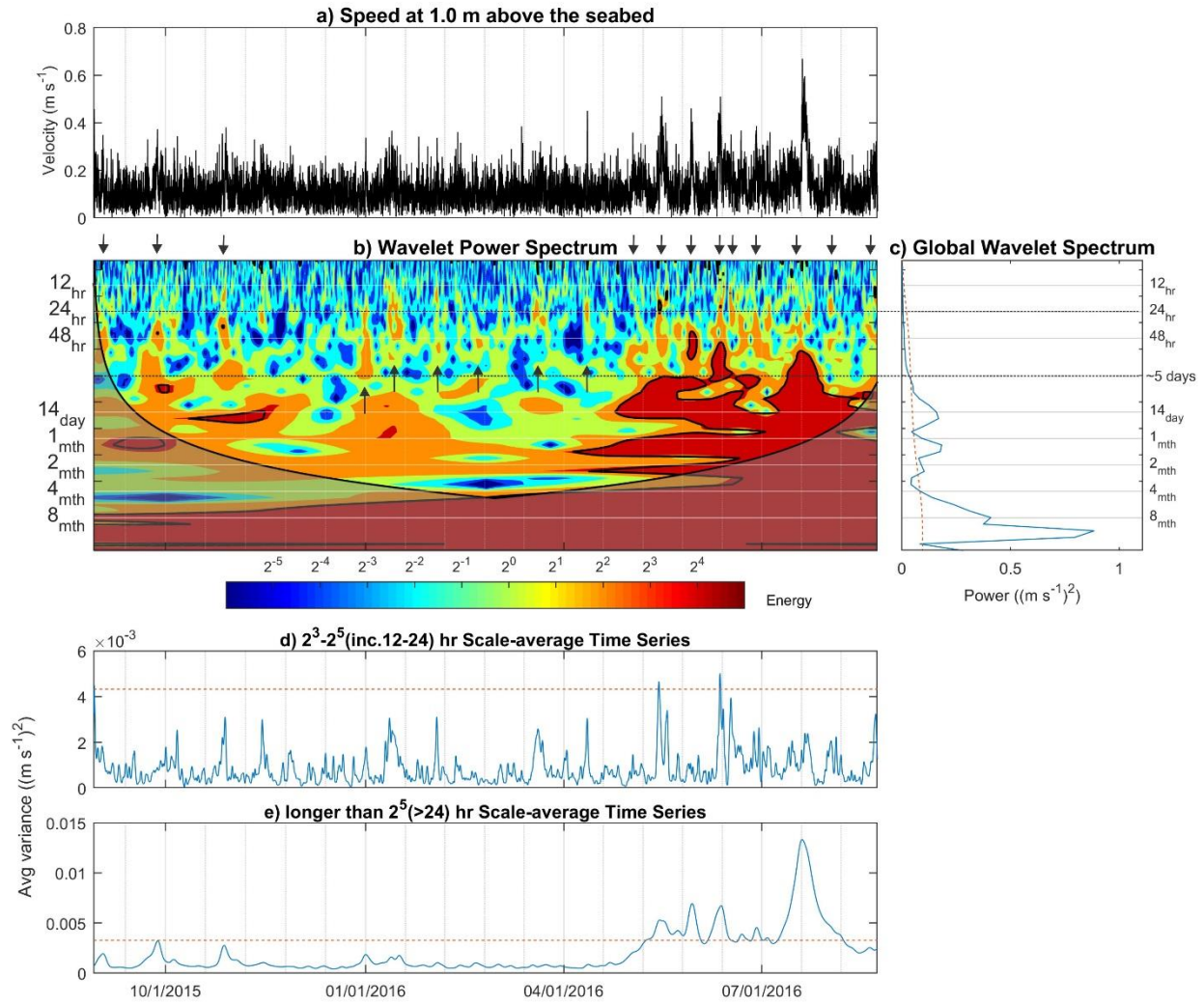
Figure 35 Continuous wavelet power spectra of the hourly-mean current speed at 100 cm above bottom (U100). (a) is the time series of U100. (b) Wavelet power spectrum as a function of time and frequency. (c) Global power spectrum versus frequency. (d) and (e) are respectively the average variance for 8 – 32 hours (including tidal frequencies of 12 -24 hrs) and that for periods > 32 hrs. The thick black contour in (b) denotes the 5% significance level; i.e., only the areas within the thick black contour are significant. The units on the color bar scale for energy in (b) are nominal with red representing maximum and blue minimum energy. The locations of occurrence of energy patches (in orange) at the 2 – 5 days period are indicated by black arrows.
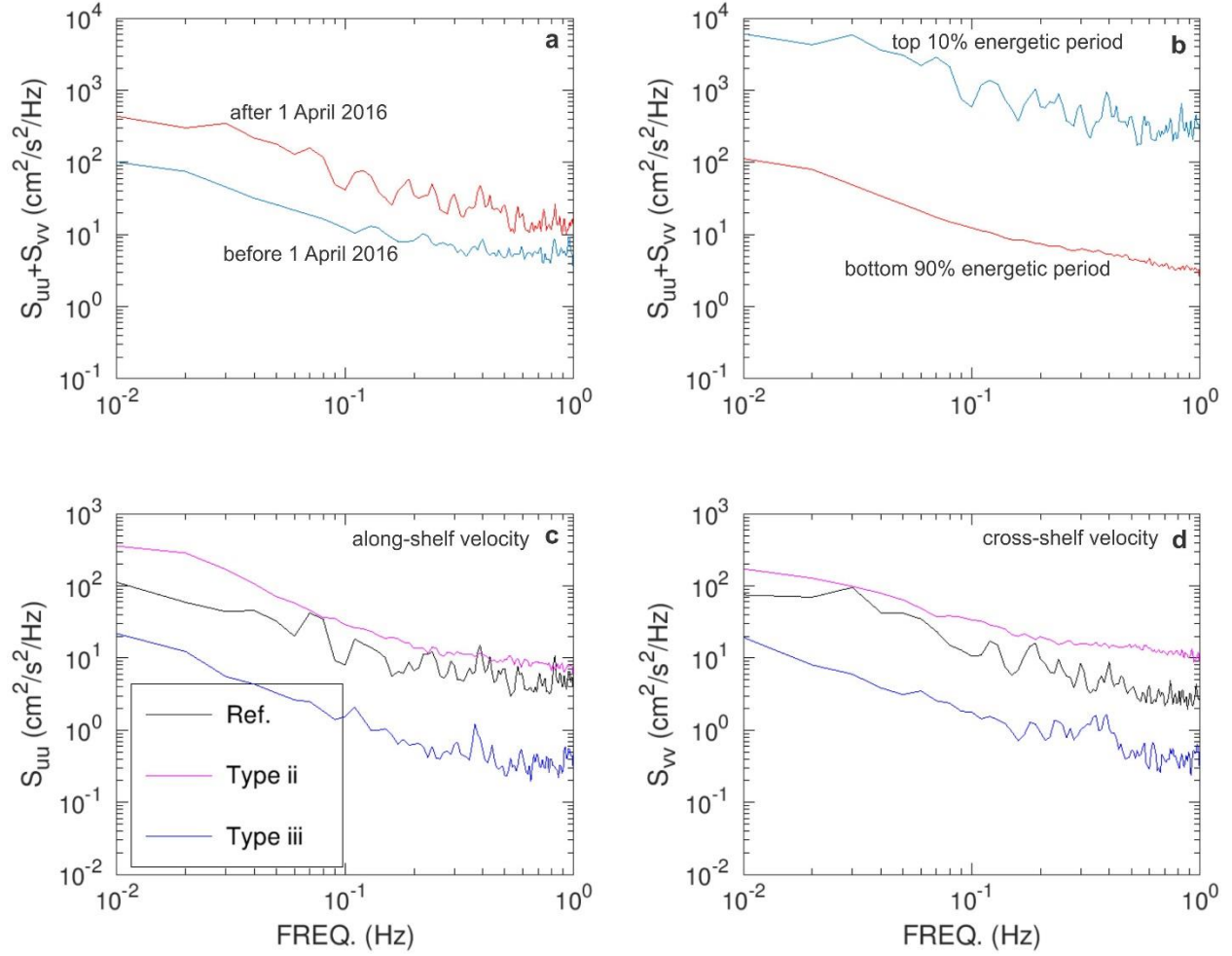
Figure 36 Top panels show the sum of the along-shelf (S_{uu}) and cross-shelf (S_{vv}) velocity spectra with (a) comparing mean spectra before 1 April 2016 (blue) and after (red), and (b) showing mean spectra of top 10% (blue) and bottom 90% (red) energetic periods. Bottom panels show mean spectra of (c) along- and (d) cross-shelf velocity components for events of Type ii (magenta), Type iii (blue) and all other reference periods (black).